symmetry

MDPI

Article

Response of Pre-Grouted Rock Masses and Joint Design of Grouting and Linings for Deep Shafts Under High Water Pressure

Yong Liu [1], Song Zhang [2,*], Wei Li [3], Wenzhu Ma [4], Xiaomin Zhou [1] and Jie Dong [2]

[1] School of Future Cities, University of Science and Technology Beijing, Beijing 100083, China; d202110015@xs.ustb.edu.cn (Y.L.)
[2] School of Civil Engineering, Hebei University of Architecture, Zhangjiakou 075000, China; dongjie1003@hotmail.com
[3] Hebei Zhucheng Industrial and Mining Machinery Co., Ltd., Xingtai 055450, China
[4] College of Civil Engineering, Tongji University, Shanghai 200082, China
* Correspondence: zs2291@hebiace.edu.cn

Abstract

To guide grouting and lining design for deep shafts under high water pressure, we derive a semi-analytical elastoplastic ground reaction curve assuming axisymmetric plane strain, a homogeneous grouted annulus, steady-state non-Darcy seepage, and a drained shaft wall. The Vlachopoulos–Diederichs longitudinal displacement relation for an unlined reference state is used to determine excavation-induced convergence. The equilibrium response is obtained by combining the ground reaction curve with the support characteristic curve of a linear-elastic shaft lining, and a parameter-matching method is established for a prescribed equilibrium convergence. The results show that increasing the grouting extent reduces equilibrium shaft wall convergence and lining contact pressure, with diminishing benefits from increasing grouted-zone thickness. Increasing the Young's modulus or cohesion of the grouted zone primarily reduces convergence before lining activation and has a relatively small effect on lining contact pressure. Increasing the lining activation distance reduces lining contact pressure but increases equilibrium convergence and weakens the convergence-control effect of increasing lining thickness. At a prescribed equilibrium convergence of 30.80 mm and a lining thickness of 0.60 m, increasing the grouted-zone outer radius from 7 to 9 m increases the matching lining activation distance by 49.6% and reduces lining contact pressure by 46.3%.

Keywords: deep vertical shaft; pre-grouting; non-Darcy seepage; convergence–confinement method; shaft lining; joint design

Check for updates

Academic Editor: Raffaele Barretta

Received: 24 October 2026
Revised: 11 November 2026
Accepted: 17 November 2026
Published: 20 November 2026

Copyright: © 2026 by the authors. Licensee MDPI, Basel, Switzerland. This article is an open access article distributed under the terms and conditions of the Creative Commons Attribution (CC BY) license.

1. Introduction

As mineral resource extraction extends to greater depths, high in situ stresses and complex groundwater conditions impose greater demands on rock mass stability and deformation control in underground engineering [1,2]. Shafts provide essential access between the surface and underground workings, and their construction and support schemes depend on shaft dimensions, depth, and site-specific geological and hydrogeological conditions [3]. Groundwater level, the permeability of the surrounding rock mass and lining, and leakage conditions also influence the service performance of underground structures [4]. For deep shafts in water-bearing fractured rock, pre-grouting for water control and shaft lining sup-

port require joint design to address construction inflow, rock deformation, and structural load-bearing requirements [5–7].

Pre-grouting modifies the hydraulic and mechanical properties of rock masses through fracture filling and cementation, providing both water control and reinforcement [8]. Laboratory tests have shown that cementation products can limit water ingress by filling pores or forming a dense surface layer [9–11]. Field observations from urban hard-rock tunnels have identified relationships among grouting effort, water inflow, and pore pressure changes, indicating that water-control performance should be assessed together with the pore pressure response [12]. Shear–seepage and triaxial tests provide a basis for characterizing the strength, deformation, and permeability of grouted rock [13,14]. Hydraulic studies have examined non-Darcy effects under different flow conditions, using the Hansbo and Izbash models to calculate pore pressures and inflow in grouted tunnels [15–17]. Studies of rock–lining interaction have incorporated pore pressure and seepage forces into mechanical analyses and developed hydromechanical coupling methods that account for discrete fractures and nonlinear seepage [18–20]. Ground reaction curves accounting for rock mass reinforcement have also been investigated [21]. These studies provide a computational basis for characterizing grouting performance and relating it to excavation-induced deformation and support loads.

The convergence–confinement method describes the relationship between rock mass deformation and support reaction through a combined analysis of the ground reaction curve (GRC), longitudinal displacement profile (LDP), and support characteristic curve (SCC) [22]. LDPs accounting for plastic zone extent provide an approximate representation of the spatial effect of the excavation face and relate support installation distance to convergence [23]. Shaft studies have established relationships for radial lining loads and convergence before permanent lining installation [24,25], and examined stress release, delayed support, and interactions between time-dependent rock masses and multilayer linings [26,27]. Studies of support timing in tunnel boring machine (TBM) construction have likewise treated rock deformation and support capacity as joint decision constraints [28]. These findings indicate that installation position and structural stiffness should be considered together in load and deformation analyses [29]. Comparisons between two- and three-dimensional models under large-deformation conditions or with stiff support close to the face further show that the applicability of conventional convergence–confinement methods requires case-specific assessment [30,31].

For pre-grouted shafts with drainage maintained at the shaft wall, satisfying inflow-control requirements alone does not determine the load-bearing demand on the lining. The hydraulic and mechanical improvements produced by pre-grouting must be characterized separately. Changes in lining thickness also modify contact loads and additional deformation after lining activation through their effect on structural stiffness. A consistent set of hydraulic boundary conditions and displacement references is therefore needed to quantify the combined effects of pre-grouting parameters, lining activation distance, and lining thickness on final contact loads and shaft wall convergence, and to identify design combinations that satisfy water-control, deformation, and load-bearing requirements.

This study examines pre-grouted deep shafts in rock formations under high water pressure. A GRC is constructed from non-Darcy seepage and elastoplastic rock mass solutions under axisymmetric, steady-state seepage conditions with drainage at the shaft wall. The unlined reference state for the same grouting configuration is used with the Vlachopoulos–Diederichs longitudinal displacement relation to approximate the spatial effect of the excavation face and determine convergence at lining activation [23]. The SCC of a linear-elastic thick-walled shaft lining is then introduced, and final contact pressure and shaft wall convergence are solved jointly using the additional deformation after lining

activation. The study quantifies the combined effects of pre-grouting parameters, lining activation distance, and lining thickness on the load response, and identifies design combinations subject to inflow-control, rock deformation, and lining load-bearing constraints. The resulting method provides a computational basis for designing the pre-grouted zone and jointly selecting lining thickness and activation distance.

2. Elastoplastic Semi-Analytical Solutions for Pre-Grouted Rock Masses

2.1. Mechanical Model and Basic Assumptions

Grouting reinforcement increases the shear modulus and shear strength of the surrounding rock mass and reduces its seepage coefficient. The grouted and ungrouted zones are distinguished by their shear moduli and seepage coefficients. Hydromechanical coupling is described using the generalized Terzaghi effective stress principle [7,17], $\sigma_r' = \sigma_r - \lambda P_w$, where λ is the effective stress correction coefficient.

A shaft-centered mechanical model is established, as shown in Figure 1. The model comprises 3 regions: Region A, the grouted zone, $r_0 \le r \le r_1$; Region B, the ungrouted zone with seepage, $r_1 \le r \le r_2$; and Region C, the hydrostatic ungrouted outer region of the radially unbounded rock mass, $r_2 \le r \le r_3$. The radial total stresses at r_0, r_1, r_2, and r_3 are denoted by σ_{r0}, σ_{r1}, σ_{r2}, and σ_{r3}, respectively. The plastic zone radius is denoted by R_p. Two plastic zone configurations are considered: Case I, ($r_0 \le R_p \le r_1$), and Case II, $R_p > r_1$. Superscripts [A], [B], and [C] denote solutions in Regions A, B, and C, respectively. Superscript [RA] denotes the plastic grouted zone in Case I; [RBA] denotes the plastic grouted zone in Case II; and [RB] denotes the plastic ungrouted zone in Case II. For material parameters, $j = 1$ denotes the grouted zone and $j = 0$ denotes the ungrouted rock mass. Region C uses the ungrouted rock mass parameters. Parameters without a material subscript take the values for the region concerned. Superscript [AB] is a generic designation for solutions in either Region A or Region B. The main symbols and their units are listed in the Nomenclature section.

The initial total stress in the water-bearing rock mass is σ_{r3}, and the initial pore water pressure is P_{wC}. In hydrostatic Region C, P_{w2}, P_{w3}, and P_{wC} denote the same pore pressure. When water pressure acts at the inner boundary of the rock mass, the total support pressure at this boundary is $P = P_{vir} + P_L + P_{in}$, where P_{in} is the water pressure associated with a water-filled shaft or water retained by a watertight lining. When the lining is not treated as a water barrier, $P_{in} = 0$. Although P_{in} and P_{w0} act at the same location and have equal magnitudes, they represent different physical quantities.

The basic assumptions are as follows:

An axisymmetric plane-strain model of a radially unbounded rock mass is adopted. The surrounding rock mass and grouted material are treated as isotropic porous media. The grout curtain is idealized as a cylindrical zone concentric with the shaft cross-section.

To analyze the interaction between the grouted rock mass and the shaft lining under prescribed hydraulic conditions, we use a one-way coupled hydromechanical model. For each case, we specify the hydraulic parameters separately for the grouted and ungrouted zones. We assume that the parameters in each zone remain constant during excavation-induced unloading. Following the approach used in previous studies [18,32], we first solve for the steady-state pore pressure distribution using the nonlinear Izbash flow law. We then calculate the elastoplastic response of the rock mass using the generalized form of Terzaghi's effective stress principle.

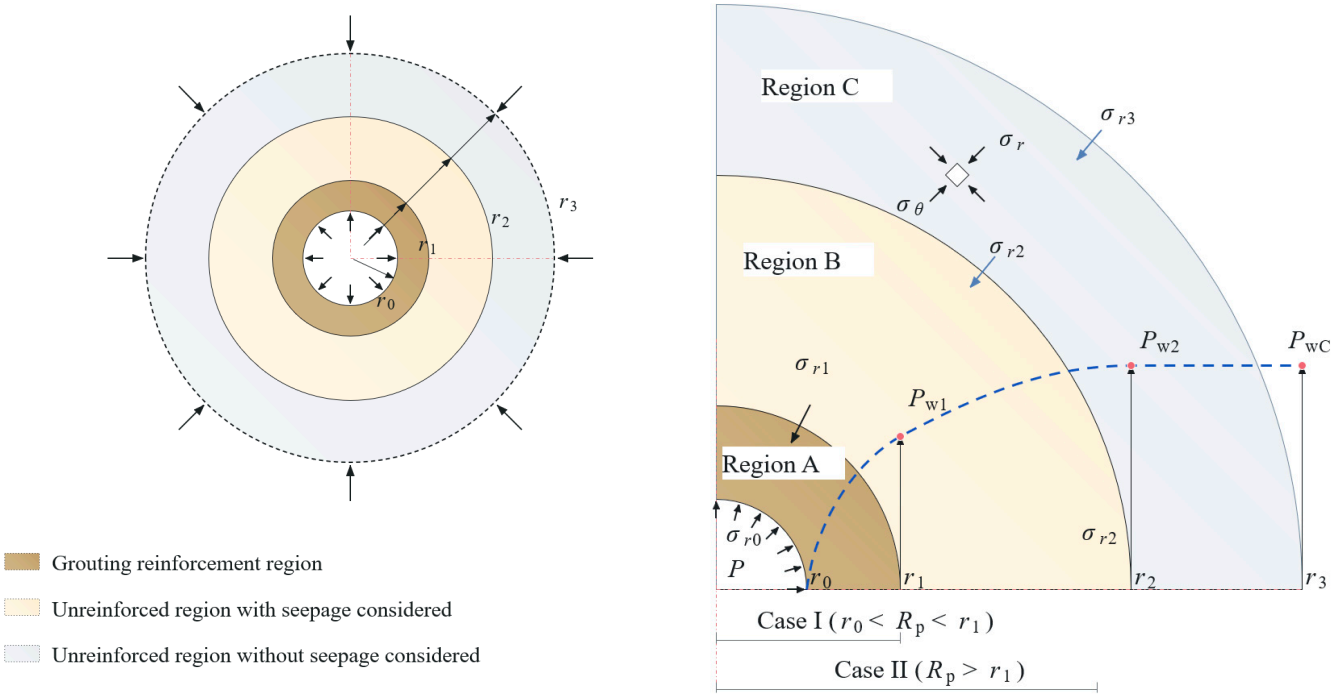


Figure 1. Mechanical model and pore pressure distribution around a pre-grouted shaft. The boundary arrows indicate radial loading. The black dashed circle marks the outer boundary at r_3, the blue dashed curve shows the pore pressure profile, and the small square shows the radial and circumferential stresses on a rock element.

2.2. Analytical Solution for Radial Seepage

Seepage through the surrounding rock mass is described by the Izbash law [17]:

$$q = 2\pi r\left(\frac{k}{\gamma_w}\frac{dP_w(r)}{dr}\right)^{\frac{1}{m}} \tag{1}$$

Here, γ_w is the unit weight of water; $P_w(r)$ is the pore water pressure distribution; r is the radial coordinate; q is the inflow per unit shaft depth; m is the non-Darcy exponent for the region concerned, ranging from 1.0 to 2.0 for high-velocity non-Darcy flow and increasing as specimen porosity decreases; and k is the regional Izbash seepage coefficient. The regional parameters m and k correspond to m_1 and k_1 in the grouted zone, and m_0 and k_0 in the ungrouted zone.

Under steady-state seepage, the inflow crossing each concentric cylindrical surface is equal. Combining this condition with the Izbash law gives the seepage continuity equation in terms of pore water pressure $P_w(r)$ and radial distance r:

$$\frac{dq(r)}{dr} = \frac{1}{m}\left(2\pi k^{\frac{1}{m}}\left(\left(\frac{dP_w(r)}{dr}\right)^{\frac{1-m}{m}}\gamma_w{}^{-\frac{1}{m}}\left[\left(\frac{d^2P_w(r)}{dr^2}\right)r + m\left(\frac{dP_w(r)}{dr}\right)\right]\right)\right) = 0 \tag{2}$$

Solving Equation (2) gives the general pore water pressure solution:

$$P_w(r) = -\frac{r\left(-\frac{C_{1w}}{r}\right)^m\gamma_w}{(m-1)k} + C_{2w} \tag{3}$$

Pore water pressure is taken to be radially continuous across the interface between the grouted and ungrouted zones, with the following boundary conditions:

$$\begin{cases} P_w^{[A]}(r = r_0) = P_{w0} \\ P_w^{[A]}(r = r_1) = P_w^{[B]}(r = r_1) = P_{w1} \\ P_w^{[B]}(r = r_2) = P_w^{[C]}(r = r_2) = P_{w2} \\ P_w^{[C]}(r \to \infty) = P_{w2} = P_{w3} \end{cases} \tag{4}$$

The grouted zone is assigned a seepage coefficient k_1 and non-Darcy exponent m_1, whereas the corresponding parameters for the ungrouted rock mass are k_0 and m_0. Applying the boundary conditions to the general solution gives:

$$\begin{cases} P_w^{[A]}(r) = -r\left(-C_{1w}^{[A]}/r\right)^{m_1}\gamma_w[(m_1-1)k_1]^{-1} + C_{2w}^{[A]} \\ P_w^{[B]}(r) = -r\left(-C_{1w}^{[B]}/r\right)^{m_0}\gamma_w[(m_0-1)k_0]^{-1} + C_{2w}^{[B]} \\ P_w^{[C]}(r) = P_{wC} \end{cases} \tag{5}$$

The hydraulic integration constants $C_{1w}{}^{[AB]}$ and $C_{2w}{}^{[AB]}$ are distinct from C_1 and C_2 in the subsequent displacement solutions. Their expressions are given in Equation (6):

$$\begin{cases} C_{1w}^{[AB]} = -r_{i+1}\exp\left(\ln\left(\frac{r_i}{r_{i+1}}\right) + \frac{1}{m_j}\ln\left((m_j-1)k_j(P_{wi} - P_{w(i+1)})\left[\gamma_w\left(r_{i+1}\exp\left(m_j\ln\left(\frac{r_i}{r_{i+1}}\right)\right) - r_i\right)\right]^{-1}\right)\right) \\ C_{2w}^{[AB]} = r_{i+1}P_{wi}\exp\left(m_j\ln\left(\frac{r_i}{r_{i+1}}\right)\right) - P_{w(i+1)}r_i\left[r_{i+1}\exp\left(m_j\ln\left(\frac{r_i}{r_{i+1}}\right)\right) - r_i\right]^{-1} \end{cases} \tag{6}$$

The non-Darcy exponents of the grouted zone (m_1) and the ungrouted zone (m_0) may differ. The two zones share the same steady radial inflow rate per unit shaft length, q. We determine q by setting the sum of the pressure drops across the two zones equal to $P_{w2} - P_{w0}$. Continuity of pore pressure and radial flux at $r = r_1$ then gives the following expression for the interface pore pressure P_{w1}.

$$P_{w1} = \frac{k_0P_{w2}(m_0-1)\left(r_0^{1-m_1} - r_1^{1-m_1}\right)\left(\frac{q}{2\pi}\right)^{m_1-m_0} + k_1P_{w0}(m_1-1)\left(r_1^{1-m_0} - r_2^{1-m_0}\right)}{k_0(m_0-1)\left(r_0^{1-m_1} - r_1^{1-m_1}\right)\left(\frac{q}{2\pi}\right)^{m_1-m_0} + k_1(m_1-1)\left(r_1^{1-m_0} - r_2^{1-m_0}\right)} \tag{7}$$

2.3. Elastic Effective Stress and Displacement Solutions

2.3.1. Governing Equations and Boundary Conditionsfor the Elastic Solution

In axisymmetric coordinates, the effective stress equilibrium equation based on the generalized effective stress principle applies to the rock mass outside Region [C]:

$$\frac{d(\sigma_r' + \lambda P_w)}{dr} + \frac{(\sigma_r' + \lambda P_w) - (\sigma_\theta' + \lambda P_w)}{r} = 0 \tag{8}$$

Here, σ'_θ is the hoop effective stress, and σ'_r is the radial effective stress.

The strain–displacement relations for Regions [A] and [B] are:

$$\begin{cases} \varepsilon_r = \frac{du_r(r)}{dr} \\ \varepsilon_\theta = \frac{u_r(r)}{r} \end{cases} \tag{9}$$

Here, ε_r and ε_θ are the radial and hoop strains of the rock mass, respectively.

The elastic constitutive relations for the grouted rock mass are:

$$\begin{cases} (\sigma_\theta - \lambda P_w(r)) - (\sigma_{r3} - \lambda P_{w3}) = 2G(1+\mu)\varepsilon_\theta + 2G\mu\varepsilon_r \\ (\sigma_r - \lambda P_w(r)) - (\sigma_{r3} - \lambda P_{w3}) = 2G(1+\mu)\varepsilon_r + 2G\mu\varepsilon_\theta \end{cases} \tag{10}$$

Here, G is the shear modulus, $G = \frac{E}{2(1+\nu)}$; μ is an auxiliary elastic parameter, $\mu = \frac{\nu}{1-2\nu}$; ν is Poisson's ratio; and E is Young's modulus.

The radial total stress boundary conditions are:

$$\begin{cases} \sigma_r^{[A]}(r=r_0)=\sigma_{r0}=P \\ \sigma_r^{[A]}(r=r_1)=\sigma_r^{[B]}(r=r_1)=\sigma_{r1} \\ \sigma_r^{[B]}(r=r_2)=\sigma_r^{[C]}(r=r_2)=\sigma_{r2} \\ \sigma_r^{[C]}(r\to\infty)=\sigma_{r3} \end{cases} \tag{11}$$

The displacement continuity conditions are:

$$\begin{cases} u_r^{[A]}(r=r_1)=u_r^{[B]}(r=r_1) \\ u_r^{[B]}(r=r_2)=u_r^{[C]}(r=r_2) \end{cases} \tag{12}$$

2.3.2. Solutions for Regions A and B

Substituting the strain–displacement relations in Equation (9) into the constitutive relations in Equation (10), eliminating the strain terms, and then using the equilibrium equation in Equation (8) gives the general displacement solution:

$$u_r^{[AB]}=C_1^{[AB]}r+\frac{C_2^{[AB]}}{r}+r^2\left(-\frac{C_{1w}^{[AB]}}{r}\right)^{m_j}N^{[AB]} \tag{13}$$

Here, $N^{[AB]}=-\frac{\lambda_j\gamma_w}{2G_jk_j(m_j-1)(m_j-3)(1+\mu_j)}$, and C_1 and C_2 are integration constants.

Substituting Equation (13) into Equation (9), inserting Equation (9) into Equation (10), and applying the stress boundary conditions in Equation (11) gives the constants in Equation (13):

$$\begin{cases} C_1=D_1\sigma_{r(i+1)}-D_2\sigma_{ri}-D_3 \\ C_2=D_4\sigma_{r(i+1)}+D_5\sigma_{ri}+D_6 \end{cases} \tag{14}$$

The coefficients D_1–D_6 are given by:

$$\begin{cases} D_1=\frac{F_1}{F_1F_5-F_2F_4}, D_2=-\frac{F_4}{F_1F_5-F_2F_4} \\ D_3=-\frac{F_1F_6-F_3F_4}{F_1F_5-F_2F_4}, D_4=-\frac{F_2}{F_1F_5-F_2F_4} \\ D_5=\frac{F_3}{F_1F_5-F_2F_4}, D_6=\frac{F_2F_6-F_3F_5}{F_1F_5-F_2F_4} \end{cases} \tag{15}$$

The coefficients F_1–F_6 are given by:

$$\begin{cases} F_1=\left(-\frac{2G_j(1+\mu_j)}{r_i^2}+\frac{2G_j\mu_j}{r_i^2}\right), F_2=\left(2G_j(1+\mu_j)+2G_j\mu_j\right) \\ F_3=2G_j(1+\mu_j)\left(-r_i\left(-\frac{C_{1w}^{[AB]}}{r_i}\right)^{m_j}m_jN^{[AB]}+2r_i\left(-\frac{C_{1w}^{[AB]}}{r_i}\right)^{m_j}N^{[AB]}\right) \\ +2G_j\mu_jr_i\left(-\frac{C_{1w}^{[AB]}}{r_i}\right)^{m_j}N^{[AB]}+\sigma_{r3}-\lambda_jP_{w3}+\lambda_j\left(-r_i\left(-\frac{C_{1w}^{[AB]}}{r_i}\right)^{m_j}\gamma_w\left[(m_j-1)k_j\right]^{-1}+C_{2w}^{[AB]}\right) \\ F_4=\left(-\frac{2G_j(1+\mu_j)}{r_{i+1}{}^2}+\frac{2G_j\mu_j}{r_{i+1}{}^2}\right), F_5=\left(2G_j(1+\mu_j)+2G_j\mu_j\right) \\ F_6=2G_j(1+\mu_j)\left(2r_{i+1}\left(-\frac{C_{1w}^{[AB]}}{r_{i+1}}\right)^{m_j}N^{[AB]}-r_{i+1}\left(-\frac{C_{1w}^{[AB]}}{r_{i+1}}\right)^{m_j}m_jN^{[AB]}\right) \\ +2G_j\mu_jr_{i+1}\left(-\frac{C_{1w}^{[AB]}}{r_{i+1}}\right)^{m_j}N^{[AB]}+\sigma_{r3}-\lambda_jP_{w3}+\lambda_j\left(-r_{i+1}\left(-\frac{C_{1w}^{[AB]}}{r_{i+1}}\right)^{m_j}\gamma_w\left[(m_j-1)k_j\right]^{-1}+C_{2w}^{[AB]}\right) \end{cases} \tag{16}$$

For Region A, $i=0$ and $j=1$; for Region B, $i=1$ and $j=0$.

2.3.3. Solution for Region C

In the ungrouted Region [C], where seepage effects are excluded, a dimensionless radius ω is introduced. The quantity ω_{r2} denotes the value of ω at $r=r_2$:

$$\omega=\frac{r_0}{r} \tag{17}$$

The equilibrium equation is:

$$\frac{d\sigma_r(\omega)}{d\omega} - \frac{\sigma_r(\omega) - \sigma_\theta(\omega)}{\omega} = 0 \tag{18}$$

The strain–displacement relations are:

$$\begin{cases} \varepsilon_\theta(\omega) = \frac{\omega}{r_0} u_r(\omega) \\ \varepsilon_r(\omega) = -\frac{\omega^2}{r_0} \frac{du_r(\omega)}{d\omega} \end{cases} \tag{19}$$

Combining the strain–displacement relations in Equation (19), the equilibrium equation in Equation (18), and the constitutive relations in Equation (10) yields the displacement-based equilibrium equation:

$$\omega^2 \frac{d^2 u_r^{[C]}(\omega)}{d\omega^2} + \omega \frac{du_r^{[C]}(\omega)}{d\omega} - u_r^{[C]}(\omega) = 0 \tag{20}$$

Solving Equation (20) gives:

$$u_r^{[C]}(\omega) = \frac{C_1^{[C]}}{\omega} + C_2^{[C]}\omega \tag{21}$$

The integration constants are obtained by combining the general displacement solution in Equation (21), the strain–displacement relations in Equation (19), the constitutive relations in Equation (10), and the stress boundary conditions in Equation (11):

$$\begin{cases} C_1{}^{[C]} = -\frac{r_0(\sigma_{r2} - \sigma_{r3})}{2\omega_{r2}{}^2 G_0} \\ C_2{}^{[C]} = 0 \end{cases} \tag{22}$$

The radial stresses at the regional interfaces remain unknown in the displacement solutions. Substituting Equations (13) and (21) into the displacement continuity conditions in Equation (12) gives expressions for σ_{r1} and σ_{r2}. Inserting these interface stresses into the integration constants determines the displacement in each region. The strains are then obtained from the strain–displacement relations, and substitution into the constitutive relations gives the corresponding effective stresses.

2.4. Plastic Effective Stress and Displacement Solutions

2.4.1. Governing Equations and Boundary Conditions for the Plastic Solution

The elastic hoop and radial effective stresses at each radial position are substituted into the strength criterion to locate the plastic zone boundary, whose radial coordinate is R_p. Within the plastic zone, the displacement and stress fields no longer satisfy the elastic governing equations. The affine transformation in Equation (23) maps the physical domain to a normalized domain:

$$\rho = \frac{r}{R_p} \tag{23}$$

After the affine transformation, first derivatives of the mechanical variables with respect to the radial coordinate r are expressed as:

$$\begin{cases} \frac{\partial(\,)}{\partial r} = \frac{1}{R_p} \frac{d(\,)}{d\rho} \\ \frac{\partial(\,)}{\partial R_p} = -\frac{\rho}{R_p} \frac{d(\,)}{d\rho} = \dot{(\,)} \end{cases} \tag{24}$$

Incremental plasticity requires a specified loading–unloading path [33]. Changes in mechanical variables can therefore be evaluated through their first derivatives with respect to the loading or unloading parameter. During shaft excavation, the loading path is represented by a continuous reduction in virtual support pressure, accompanied by

monotonic expansion of the plastic zone radius R_p. The rates of the mechanical variables are accordingly expressed through first derivatives with respect to R_p. Throughout the following derivation, an overdot denotes a first derivative with respect to R_p.

The total strain rates are decomposed into elastic and plastic components in Equation (25). These components are governed by Hooke's law and the plastic potential, as given in Equations (26) and (27), respectively.

The total strain rate decomposition is:

$$\begin{cases} \dot{\varepsilon}_r = \dot{\varepsilon}_r^e + \dot{\varepsilon}_r^p \\ \dot{\varepsilon}_\theta = \dot{\varepsilon}_\theta^e + \dot{\varepsilon}_\theta^p \end{cases} \tag{25}$$

Here, $\dot{\varepsilon}_r$ and $\dot{\varepsilon}_\theta$ are the total radial and hoop strain rates, respectively; $\dot{\varepsilon}_r^e$ and $\dot{\varepsilon}_\theta^e$ are their elastic components; and $\dot{\varepsilon}_r^p$ and $\dot{\varepsilon}_\theta^p$ are their plastic components.

The elastic strain rate components are expressed using Hooke's law:

$$\begin{cases} \dot{\varepsilon}_r^e = \frac{1-\nu}{2G}\dot{\sigma}_r'^e - \frac{\nu}{2G}\dot{\sigma}_\theta'^e \\ \dot{\varepsilon}_\theta^e = \frac{1-\nu}{2G}\dot{\sigma}_\theta'^e - \frac{\nu}{2G}\dot{\sigma}_r'^e \end{cases} \tag{26}$$

Here, $\dot{\sigma}_r'^e$ and $\dot{\sigma}_\theta'^e$ are the elastic radial and hoop effective stress rates, respectively; ν is Poisson's ratio of the rock mass; and G is its shear modulus. The plastic strain rate components are expressed using the plastic potential:

$$\begin{cases} \dot{\varepsilon}_r^p = \xi\frac{\partial g}{\partial \sigma_r'} = \xi \\ \dot{\varepsilon}_\theta^p = \xi\frac{\partial g}{\partial \sigma_\theta'} = -\xi k_{\psi,j} \end{cases} \tag{27}$$

Here, ξ is the plastic multiplier, and g is the plastic potential. The expression for g is given in Equation (36).

The strain–displacement rate relations are given in Equation (28):

$$\begin{cases} \dot{\varepsilon}_r = \frac{\partial \dot{u}}{\partial r} \\ \dot{\varepsilon}_\theta = \frac{\dot{u}}{r} \end{cases} \tag{28}$$

Combining Equations (25)–(28) and eliminating the plastic multiplier ξ gives the displacement governing equation:

$$\frac{\partial \dot{u}_r}{\partial r} - \frac{1-\nu}{2G}\dot{\sigma}_r' + \frac{\nu}{2G}\dot{\sigma}_\theta' - \frac{\partial g/\partial \sigma_r'}{\partial g/\partial \sigma_\theta'}\left(\frac{\dot{u}_r}{r} - \frac{1-\nu}{2G}\dot{\sigma}_\theta' + \frac{\nu}{2G}\dot{\sigma}_r'\right) = 0 \tag{29}$$

After the affine transformation, the governing equation for the plastic rock mass becomes:

$$2G\rho\frac{d^2u_r}{d\rho^2} + 2G\left(k_{\psi,j} - 1\right)\frac{du_r}{d\rho} + \rho R_p\left[(\nu-1)k_{\psi,j} - \nu\right]\frac{d\sigma_\theta'}{d\rho} + R_p\rho\left(k_{\psi,j}\nu - \nu + 1\right)\frac{d\sigma_r'}{d\rho} = 0 \tag{30}$$

Because Equation (30) applies under plastic conditions, σ'_r and σ'_θ in the displacement equation must also satisfy the strength criterion in Equation (35), the consistency condition in Equation (31), and the equilibrium equation in Equation (33). These relations jointly determine the governing equation for displacement in the plastic zone.

The consistency condition is:

$$\frac{\partial f}{\partial \sigma_r'}\dot{\sigma}_r' + \frac{\partial f}{\partial \sigma_\theta'}\dot{\sigma}_\theta' = 0 \tag{31}$$

Combining the consistency condition with the Mohr–Coulomb strength criterion gives:

$$\frac{d\sigma_\theta'}{d\rho} - k_{\varphi,j}\frac{d\sigma_r'}{d\rho} = 0 \tag{32}$$

The strength coefficient is defined as $k_{\varphi,j} = \tan^2\left(\frac{\pi}{4} + \frac{\varphi_j}{2}\right)$.
The stress state in the plastic zone must also satisfy equilibrium:

$$\frac{d\sigma'_r}{d\rho} + \frac{\sigma'_r - \sigma'_\theta}{\rho} = 0 \tag{33}$$

Combining Equations (32) and (33) and eliminating the hoop effective stress gives the governing equation for radial effective stress:

$$\rho\frac{d^2\sigma'_r(\rho)}{d\rho^2} + \left(2 - k_{\varphi,j}\right)\frac{d\sigma'_r(\rho)}{d\rho} = 0 \tag{34}$$

The strength increase produced by grouting is represented using the Mohr–Coulomb criterion:

$$f = \sigma'_\theta - \tan^2\left(\frac{\pi}{4} + \frac{\varphi_j}{2}\right)\sigma'_\theta - \left(\tan^2\left(\frac{\pi}{4} + \frac{\varphi_j}{2}\right) - 1\right)\frac{c_j}{\tan\varphi_j} \tag{35}$$

Here, σ'_θ and σ'_r are the major and minor effective principal stresses, respectively; c_j is cohesion; and φ_j is the internal friction angle. The material subscript j takes values of 1 and 0 for grouted and ungrouted rock, respectively.

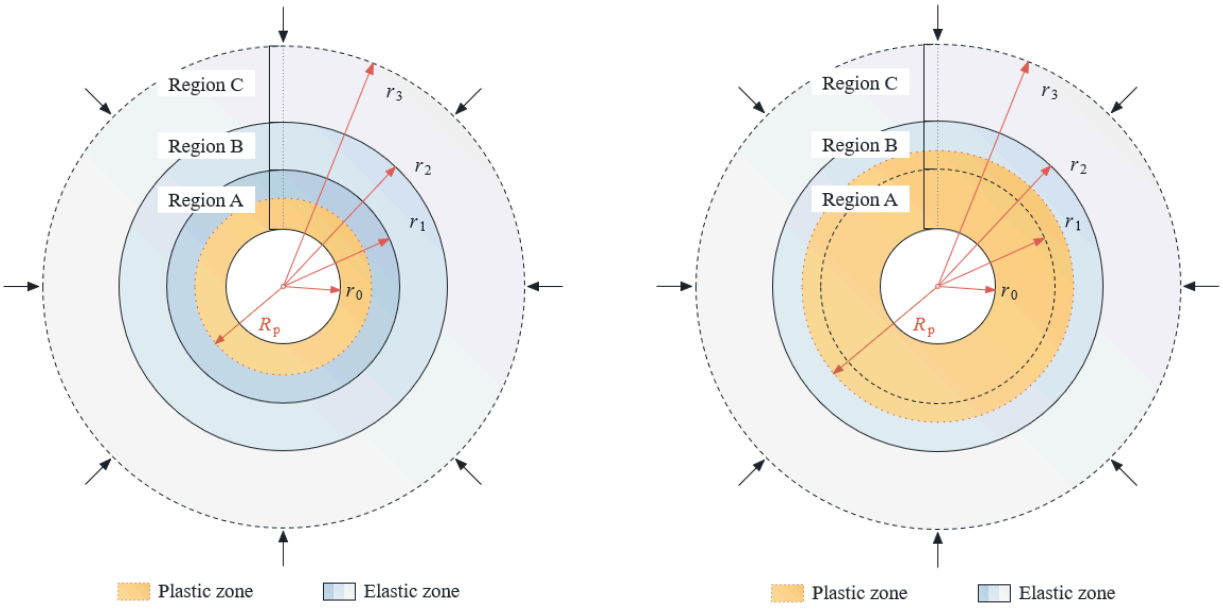
The plastic potential is:

$$g = \sigma'_\theta - k_{\psi,j}\sigma'_r \tag{36}$$

Here, $k_{\psi,j} = \tan^2(\pi/4 + \psi_j/2)$ is the dilation coefficient, and ψ_j is the dilation angle for the corresponding region. Subscripts $j = 1$ and $j = 0$ refer to the grouted zone and ungrouted rock mass, respectively.

2.4.2. Stress and Displacement Solutions for Different Plastic Zone Extents

The radial effective stress remains continuous under plastic conditions. Two plastic zone configurations are considered, as shown in Figure 2.



(**a**) Case I (**b**) Case II

Figure 2. Schematic plastic zone distributions for Cases I and II. Black arrows indicate radial loading at the outer boundary (outer dashed circle), and red arrows indicate the radii. The dotted outline of the yellow zone marks the plastic front. In (**b**), the inner dashed circle marks the outer boundary of the grouted zone.

In Case I, the plastic zone is confined to the grouted zone ($r_0 \le R_p \le r_1$). The effective stress boundary conditions are:

$$\begin{cases} \sigma_r'^{[RA]}(r = r_0) = P \\ \sigma_r'^{[RA]}\left(r = R_p\right) = \sigma_r'^{[A]}\left(r = R_p\right) \end{cases} \tag{37}$$

In Case II, the plastic zone extends into the ungrouted rock mass ($R_p > r_1$). The effective stress boundary conditions are:

For the grouted zone:

$$\begin{cases} \sigma_r'^{[RBA]}(r = r_0) = P \\ \sigma_r'^{[RBA]}(r = r_1) = \sigma_r'^{[RB]}(r = r_1) \end{cases} \tag{38}$$

For the ungrouted zone:

$$\begin{cases} \sigma_r'^{[RBA]}(r = r_1) = \sigma_r'^{[RB]}(r = r_1) \\ \sigma_r'^{[RB]}\left(r = R_p\right) = \sigma_r'^{[B]}\left(r = R_p\right) \end{cases} \tag{39}$$

Under the elastic–perfectly plastic conditions considered here, displacement and its first radial derivative are continuous at the elastic–plastic interface. Their values at the interface provide initial conditions for Runge–Kutta integration toward the shaft wall. The values obtained at each radial position are used as the initial conditions for the next integration step, yielding the displacement throughout the plastic zone. The initial displacement conditions are specified separately for the two plastic zone configurations in Figure 2:

For Case I, the initial conditions for radial displacement in the plastic zone are:

$$\begin{cases} u_r^{[RA]}\left(r = R_p, \rho = 1\right) = u_r^{[A]}\left(r = R_p\right) \\ \frac{du_r^{[RA]}}{dr}\left(r = R_p, \rho = 1\right) = \frac{du_r^{[A]}}{dr}\left(r = R_p\right) \end{cases} \tag{40}$$

For Case II, the initial conditions for radial displacement in the plastic zone are:

$$\begin{cases} u_r^{[RBA]}(r = r_1) = u_r^{[RB]}(r = r_1) \\ \frac{du_r^{[RBA]}}{dr}(r = r_1) = \frac{du_r^{[RB]}}{dr}(r = r_1) \\ u_r^{[RB]}\left(r = R_p, \rho = 1\right) = u_r^{[B]}\left(r = R_p\right) \\ \frac{du_r^{[RB]}}{dr}\left(r = R_p, \rho = 1\right) = \frac{du_r^{[B]}}{dr}\left(r = R_p\right) \end{cases} \tag{41}$$

The plastic zone solutions are derived separately for the two cases. For Case I:

Solving Equation (34) gives the general radial effective stress solution in Region [RA]:

$$\sigma_r'^{[RA]}(\rho) = C_1^{[RA]} + C_2^{[RA]}\rho^{-1+k_{\varphi,1}} \tag{42}$$

Using the strength criterion in Equation (35), the hoop effective stress in Region [RA] is:

$$\sigma_\theta'^{[RA]}(\rho) = k_{\varphi,1}\sigma_r'^{[RA]} + \left(k_{\varphi,1} - 1\right)\frac{c_1}{\tan\varphi_1} \tag{43}$$

Substituting Equation (42) into the boundary conditions in Equation (37) gives the integration constants:

$$\begin{cases} C_1^{[RA]} = \left[\sigma_r'^{[A]}\left(r = R_p\right)\left(\frac{r_0}{R_p}\right)^{-1+k_{\varphi,1}} - P\right]\left[\left(\frac{r_0}{R_p}\right)^{-1+k_{\varphi,1}} - 1\right]^{-1} \\ C_2^{[RA]} = \left[P - \sigma_r'^{[A]}\left(r = R_p\right)\right]\left[\left(\frac{r_0}{R_p}\right)^{-1+k_{\varphi,1}} - 1\right]^{-1} \end{cases} \tag{44}$$

Differentiating Equations (42) and (43) with respect to ρ gives the analytical expressions for $\frac{d\sigma_r'^{[RA]}}{d\rho}$ and $\frac{d\sigma_\theta'^{[RA]}}{d\rho}$:

$$\begin{cases} \frac{d\sigma_r'^{[RA]}}{d\rho} = \frac{C_2^{[RA]}\rho^{-1+k_{\varphi,1}(-1+k_{\varphi,1})}}{\rho} \\ \frac{d\sigma_\theta'^{[RA]}}{d\rho} = k_{\varphi,1}\left[\frac{C_2^{[RA]}\rho^{-1+k_{\varphi,1}(-1+k_{\varphi,1})}}{\rho}\right] \end{cases} \tag{45}$$

Substituting Equation (45) into Equation (30) gives the plastic displacement governing equation for Region [RA], Equation (46). The displacement is obtained by Runge–Kutta integration using the boundary conditions in Equation (40).

$$2G_1\rho\frac{d^2u_r^{[RA]}}{d\rho^2}+2G_1\left(k_{\psi,1}-1\right)\frac{du_r^{[RA]}}{d\rho}+\rho R_p\left[(\nu_1-1)k_{\psi,1}-\nu_1\right]\frac{d\sigma_\theta'^{[RA]}}{d\rho}+R_p\rho\left(k_{\psi,1}\nu_1-\nu_1+1\right)\frac{d\sigma_r'^{[RA]}}{d\rho}=0 \tag{46}$$

For Case II:

Excavation unloading directly reduces radial confinement at the shaft wall. We assume that yielding begins in the grouted rock mass at the shaft wall and that the plastic zone expands continuously outward as unloading proceeds. The plastic zone radius R_p defines its extent. In Case II, the plastic front has advanced beyond the outer boundary of the grouted zone ($R_p > r_1$). At this stage, the entire grouted zone has yielded. This solution does not apply if a separate plastic zone develops in the ungrouted rock before the advancing front reaches the interface. Equations (29) and (34) govern displacement and radial effective stress in Case II, respectively. Equation (41) gives the displacement boundary conditions.

A local dimensionless radial coordinate $\eta = r/r_1$ is used in the grouted zone for Case II. This coordinate is denoted consistently by η to distinguish it from ρ, which is normalized by the plastic zone radius. The radial effective stress solution is:

$$\sigma_r'^{[RBA]}(\eta)=C_1^{[RBA]}+C_2^{[RBA]}\eta^{-1+k_{\varphi,1}} \tag{47}$$

The strength criterion gives the hoop effective stress in the grouted zone for Case II:

$$\sigma_\theta'^{[RBA]}(\eta)=k_{\varphi,1}\sigma_r'^{[RBA]}+\left(k_{\varphi,1}-1\right)\frac{c_1}{\tan\varphi_1} \tag{48}$$

The integration constants are:

$$\begin{cases} C_1^{[RBA]}=\left[\sigma_r'^{[RB]}(r=r_1)\left(\frac{r_0}{r_1}\right)^{-1+k_{\varphi,1}}-P\right]\left[\left(\frac{r_0}{r_1}\right)^{-1+k_{\varphi,1}}-1\right]^{-1} \\ C_2^{[RBA]}=\left[P-\sigma_r'^{[RB]}(r=r_1)\right]\left[\left(\frac{r_0}{r_1}\right)^{-1+k_{\varphi,1}}-1\right]^{-1} \end{cases} \tag{49}$$

Differentiating Equations (47) and (48) with respect to η gives the analytical expressions for $\frac{d\sigma_r'^{[RBA]}}{d\eta}$ and $\frac{d\sigma_\theta'^{[RBA]}}{d\eta}$:

$$\begin{cases} \frac{d\sigma_r'^{[RBA]}}{d\eta}=\frac{C_2^{[RBA]}\eta^{-1+k_{\varphi,1}}\left(-1+k_{\varphi,1}\right)}{\eta} \\ \frac{d\sigma_\theta'^{[RBA]}}{d\eta}=k_{\varphi,1}\left[\frac{C_2^{[RBA]}\eta^{-1+k_{\varphi,1}}\left(-1+k_{\varphi,1}\right)}{\eta}\right] \end{cases} \tag{50}$$

Using the local coordinate $\eta = r/r_1$ in the grouted zone gives the displacement governing equation in Equation (51):

$$2G_1\eta\frac{d^2u_r^{[RBA]}}{d\eta^2}+2G_1\left(k_{\psi,1}-1\right)\frac{du_r^{[RBA]}}{d\eta}+\eta r_1\left[(\nu_1-1)k_{\psi,1}-\nu_1\right]\frac{d\sigma_\theta'^{[RBA]}}{d\eta}+r_1\eta\left(k_{\psi,1}\nu_1-\nu_1+1\right)\frac{d\sigma_r'^{[RBA]}}{d\eta}=0 \tag{51}$$

To account for the different strength parameters of the grouted and ungrouted rock, the radial effective stress equation for the ungrouted zone in Case II is written as follows. The ungrouted plastic zone uses the dimensionless coordinate $\rho = r/R_p$.

$$\rho\frac{d^2\sigma_r'(\rho)}{d\rho^2}+\left(2-k_{\varphi,0}\right)\frac{d\sigma_r'(\rho)}{d\rho}=0 \tag{52}$$

Here, $k_{\varphi,0}=\tan^2\left(\frac{\pi}{4}+\frac{\varphi_0}{2}\right)$.

Solving Equation (52) gives the general radial effective stress solution for the ungrouted zone in Case II:

$$\sigma_r'^{[RB]}(\rho) = C_1^{[RB]} + C_2^{[RB]}\rho^{-1+k_{\varphi,0}} \tag{53}$$

Using the strength criterion in Equation (35), the hoop effective stress in the ungrouted zone for Case II is:

$$\sigma_\theta'^{[RB]}(\rho) = k_{\varphi,0}\sigma_r'^{[RB]} + \left(k_{\varphi,0} - 1\right)a_0 \tag{54}$$

Here, $k_{\varphi,0} = \tan^2\left(\frac{\pi}{4} + \frac{\varphi_0}{2}\right)$, and $a_0 = \frac{c_0}{\tan\varphi_0}$.

Substituting Equation (53) into the boundary conditions in Equation (39) gives the integration constants in Equations (53) and (54):

$$\begin{cases} C_1^{[RB]} = \left[\sigma_r'^{[B]}\left(r = R_p\right)\left(\frac{r_1}{R_p}\right)^{-1+k_{\varphi,0}} - \sigma_r'^{[RB]}(r = r_1)\right]\left[\left(\frac{r_1}{R_p}\right)^{-1+k_{\varphi,0}} - 1\right]^{-1} \\ C_2^{[RB]} = \left[\sigma_r'^{[RB]}(r = r_1) - \sigma_r'^{[B]}\left(r = R_p\right)\right]\left[\left(\frac{r_1}{R_p}\right)^{-1+k_{\varphi,0}} - 1\right]^{-1} \end{cases} \tag{55}$$

Differentiating Equations (53) and (54) with respect to ρ gives the analytical expressions for $\frac{d\sigma_r'^{[RB]}}{d\rho}$ and $\frac{d\sigma_\theta'^{[RB]}}{d\rho}$:

$$\begin{cases} \frac{d\sigma_r'^{[RB]}}{d\rho} = \frac{C_2^{[RB]}\rho^{-1+k_{\varphi,0}}\left(-1+k_{\varphi,0}\right)}{\rho} \\ \frac{d\sigma_\theta'^{[RB]}}{d\rho} = k_{\varphi,0}\left[\frac{C_2^{[RB]}\rho^{-1+k_{\varphi,0}}\left(-1+k_{\varphi,0}\right)}{\rho}\right] \end{cases} \tag{56}$$

Substituting Equation (56) into Equation (30) gives the plastic displacement governing equation for Region [RB], Equation (57). The displacement is obtained by Runge–Kutta integration using the boundary conditions in Equation (41).

$$2G_0\rho\frac{d^2u_r^{[RB]}}{d\rho^2} + 2G_0\left(k_{\psi,0} - 1\right)\frac{du_r^{[RB]}}{d\rho} + \rho R_p\left[(\nu_0 - 1)k_{\psi,0} - \nu_0\right]\frac{d\sigma_\theta'^{[RB]}}{d\rho} + R_p\rho\left(k_{\psi,0}\nu_0 - \nu_0 + 1\right)\frac{d\sigma_r'^{[RB]}}{d\rho} = 0 \tag{57}$$

3. Construction and Numerical Validation of GRCs for Pre-Grouted Rock Masses

3.1. Solution Procedure for the Plastic Zone Extent

The solution procedure combines the elastoplastic effective stress and displacement solutions under hydromechanical coupling. Rock mass deformation and stability are characterized by the GRC and plastic zone radius (R_p). The main computational steps are:

Step 1: Implement the elastoplastic effective stress solutions in MATLAB R2024a.

Step 2: Calculate the elastic effective stresses at successively decreasing virtual support pressures.

Step 3: Substitute the effective stresses at $r = r_0$ into the strength criterion in Equation (35) to determine whether the response is elastic or plastic.

Step 4: For an elastic response, calculate and record the displacement at the shaft wall, $r = r_0$, using the elastic displacement solution. For a plastic response, obtain and record the displacement at $r = r_0$ by Runge–Kutta integration of the plastic displacement equation.

Step 5: Decrease the virtual support pressure P_{vir} iteratively and extract the corresponding radial shaft wall convergence $u_r(r_0)$. Plotting pressure against convergence gives the GRC of the pre-grouted rock mass. The workflow is shown in Figure 3.

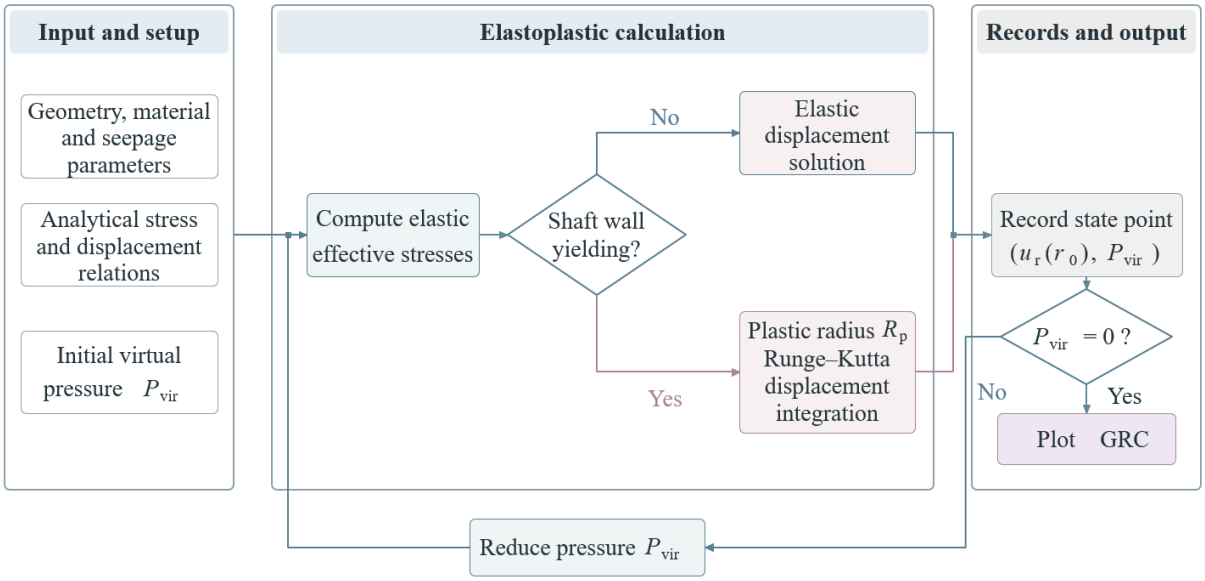


Figure 3. Workflow for constructing the GRC of a pre-grouted rock mass.

3.2. Finite Element Validation of the Semi-Analytical Solution

The water-bearing fractured rock encountered in the new main shaft of Xincheng Gold Mine, Shandong Gold, is used as the case-study background [7]. A 45° sector plane-strain model is established in Abaqus; the model and mesh are shown in Figure 4. The excavation radius is 3.75 m, the grouted-zone outer radius is 8 m, and the recharge and mechanical outer boundary radii are 35 m and 70 m, respectively. The rock mass is modeled as an elastic–perfectly plastic Mohr–Coulomb material. Table 1 lists the material parameters. In the baseline case, the dilation angle is set equal to the friction angle in each zone ($\psi_1 = \varphi_1 = 45°$ and $\psi_0 = \varphi_0 = 30°$). These values define the associated-flow reference case for comparison with cases of lower dilatancy. The mesh comprises 5040 four-node displacement–pore pressure elements (CPE4P), with local refinement near the shaft wall and shared nodes at the regional interfaces. The shaft wall is the boundary at which excavation unloading is applied, and its radial displacement is used directly to construct the GRC. The mesh was therefore locally refined near the shaft wall to better capture deformation in the adjacent rock mass. With the same material parameters, boundary conditions, and unloading procedure, the relative difference in shaft wall convergence between the original and further refined meshes did not exceed 0.1% at any of the virtual support pressures compared. The 5040-element mesh therefore provides sufficient accuracy for computing the GRC in this case. Steady-state non-Darcy seepage is solved using the Izbash relation by iteratively updating the equivalent seepage coefficient in radial element bands. The mechanical calculation proceeds through initial equilibrium, establishment of seepage, and support unloading. An amplitude function gradually reduces the virtual support pressure at the shaft wall from 15.3 MPa to 0. The initial groundwater-bearing in situ stress state is used as the displacement reference. The mean inward radial displacement of the shaft wall nodes is paired with the corresponding support pressure to construct the numerical GRC.

Figure 5 compares the semi-analytical and finite element ground reaction curves for the grouted rock mass under zero water pressure and non-Darcy seepage. The classical Kastner solution [34] for rock without pre-grouting serves as the reference. The maximum radial displacement of the shaft wall is 34.89 mm for grouted rock under zero water pressure, 36.47 mm for grouted rock under non-Darcy seepage, and 97.03 mm for the ungrouted reference case. Under zero water pressure, grouting reduces the maximum displacement by 64.04% relative to the ungrouted reference. For the grouted rock mass, non-Darcy seepage

increases the maximum displacement by 4.53% relative to the zero-water-pressure case. The elastic–plastic transition points for both grouted cases lie below and to the left of the reference transition point. They correspond to smaller critical displacements and lower virtual support pressures. In the supplementary non-Darcy seepage case, the analytical pore pressure at the interface between the grouted and ungrouted zones is 5.68 MPa. It differs from the finite element value by 3.20 kPa. At a virtual support pressure of 4 MPa, the semi-analytical and finite element solutions give shaft wall convergences of 22.38 mm and 22.53 mm, respectively. The relative error is 0.68%. At 1 MPa, the corresponding values are 32.10 mm and 33.14 mm, with a relative error of 3.24%. The two solutions agree well on the interface pore pressure and on shaft wall convergence at these two support pressures.

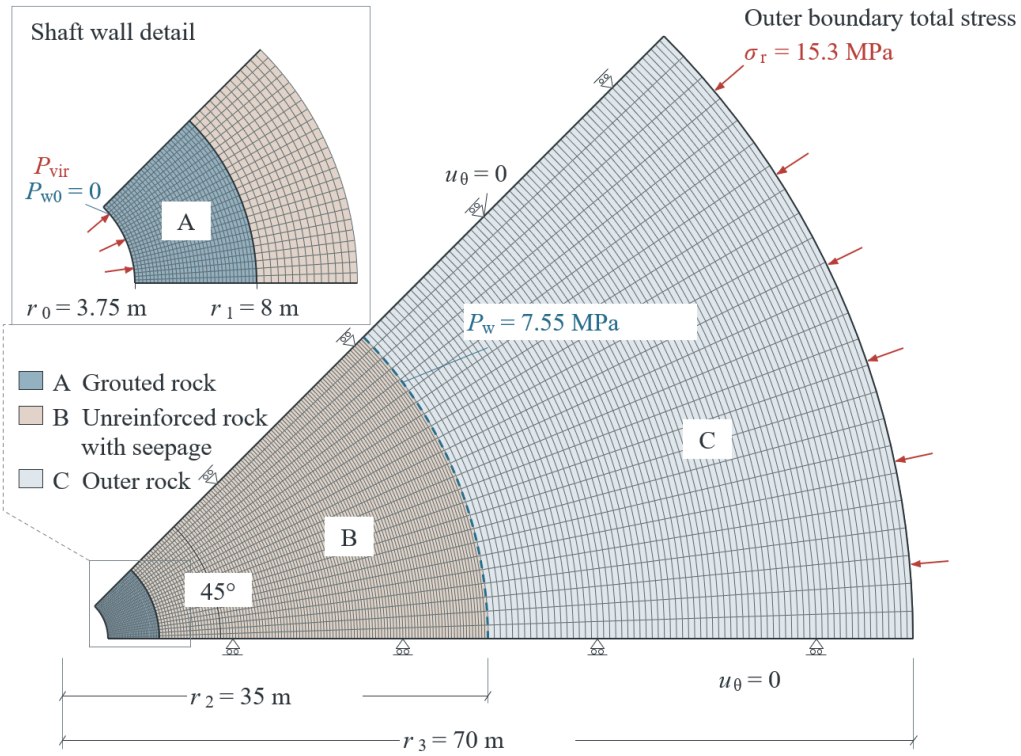


Figure 4. Finite element model, mesh, and boundary conditions. Red arrows indicate radial loading at the shaft wall and outer boundary, and blue labels give the prescribed pore pressures. Roller symbols indicate zero circumferential displacement along both radial edges.

Table 1. Parameters used in the calculations.

Elastic and Seepage Parameters		Strength Parameters		Boundary Conditions	
E_1	3.15 GPa	c_1	1.6 MPa	σ_{r3}	15.3 MPa
E_0	1.05 GPa	c_0	0.8 MPa	P_{w3}	7.55 MPa
ν_1	0.28	φ_1	45°	P_{w0}	0 MPa
ν_0	0.33	φ_0	30°	r_0	3.75 m
k_1	6.2×10^{-9} m/s	ψ_1	45°	r_1	8 m
k_0	6.2×10^{-8} m/s	ψ_0	30°		
m_1	1.05				
m_0	1.01				
λ	1.0				

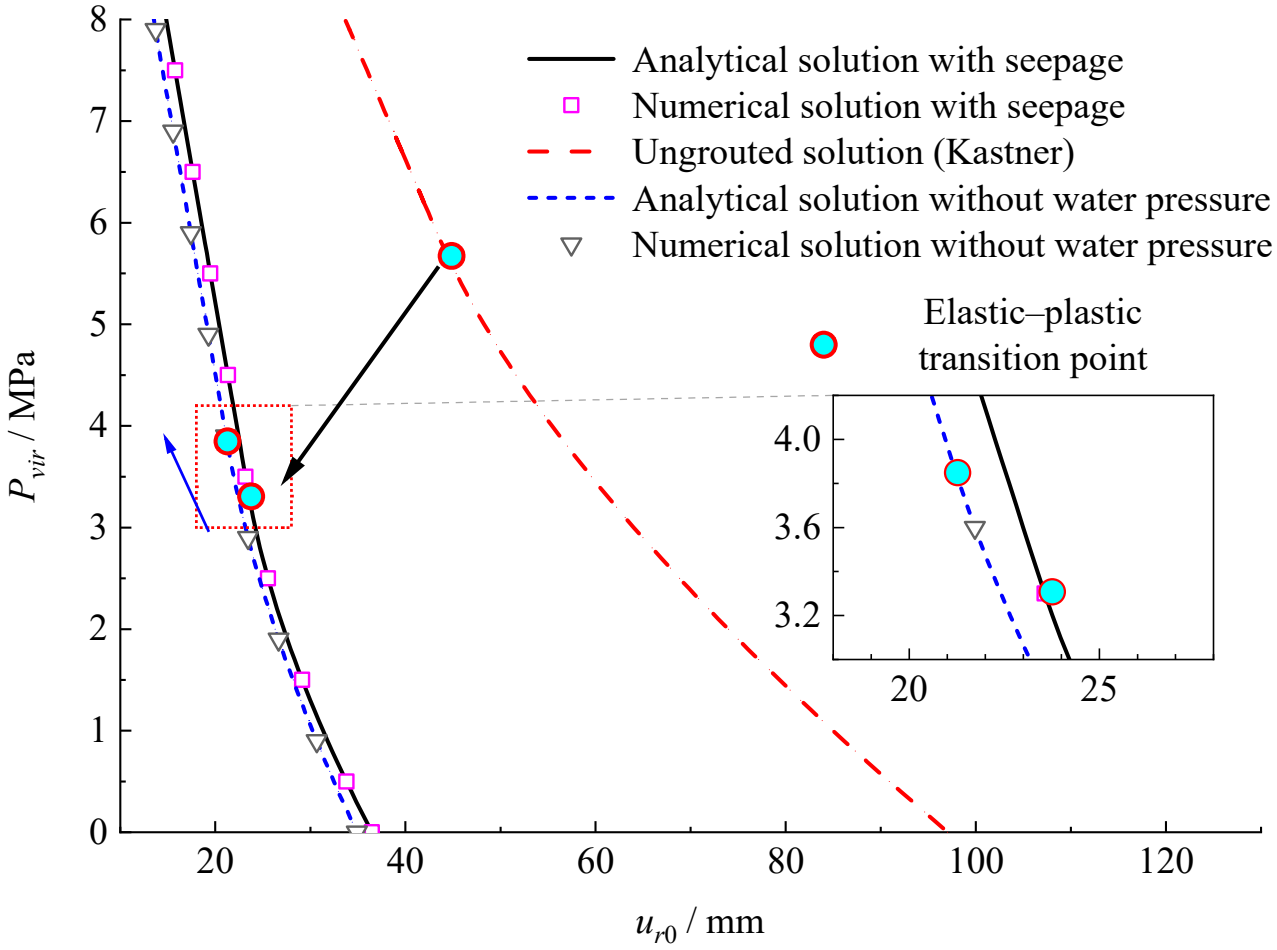


Figure 5. Finite element validation of the ground reaction curves. For grouted rock, the blue arrow indicates the shift in the elastic–plastic transition point from the case with seepage to the case without water pressure.

4. Interaction Between the Pre-Grouted Rock Mass and Shaft Lining

4.1. Lining Stiffness and Support Characteristic Curve

The shaft lining is modeled as a homogeneous, isotropic, linear-elastic thick-walled cylinder under axisymmetric plane-strain conditions, with zero radial pressure at its inner surface. Under the small-deformation assumption, the lining outer radius is taken as the excavation radius r_0, its thickness is h_L, and its inner radius is $r_0 - h_L$. The elastic thick-walled cylinder solution gives the radial stiffness at the lining outer surface:

$$K_L = \frac{E_L\left[r_0^2 - (r_0 - h_L)^2\right]}{(1+\nu_L)r_0\left[(1-2\nu_L)r_0^2 + (r_0 - h_L)^2\right]} \tag{58}$$

Here, E_L and ν_L are Young's modulus and Poisson's ratio of the lining, respectively. The stiffness K_L is the contact pressure per unit radial displacement of the outer surface and has dimensions of pressure per unit length. This stiffness expression is also given by Benato et al. [35].

The stress-free configuration at lining activation is used as the reference state, and the accumulated shaft wall convergence at that instant is denoted by u_i. When the lining remains in continuous compressive contact with the rock mass, its outer-surface displacement equals the subsequent increment in shaft wall convergence [29]. The SCC is therefore:

$$P_L = K_L[u_r(r_0) - u_i],\ u_r(r_0) \geq u_i \tag{59}$$

Here, P_L is the contact pressure at the lining outer surface, taken as positive in compression, and $u_r(r_0)$ is the accumulated radial shaft wall convergence. A specified Young's modulus is used for the load-bearing stage of the lining, without considering its age dependence.

4.2. Delayed Lining Activation and Solution of Rock–Lining Interaction

4.2.1. Longitudinal Displacement Profile and Convergence at Lining Activation

The axial coordinate originates at the shaft bottom excavation face and is positive toward the shaft collar along the excavated section. The LDP describes the short-term spatial confinement provided by the shaft bottom face, using the pre-grouted rock mass without a lining as the reference state. The geometry, material properties, and seepage conditions of this state are identical to those used for the GRC, and displacements are measured from the same initial state.

Provided that a finite zero-support-pressure solution exists, the fully unloaded shaft wall convergence and plastic zone radius are obtained from the GRC for the same case:

$$u_{\max} = u_r(r_0;P)|_{P=0}, \quad R_{p,\max} = R_p\big|_{P=0} \tag{60}$$

Here, $u_r(r_0;P)$ is the shaft wall convergence at radial boundary pressure P, and $R_{p,\max}$ is the final outer radius of the plastic zone in the unlined reference state. If this reference state remains entirely elastic, $R_{p,\max} = r_0$ is used for normalization.

For the pre-grouted circular shaft, the empirical relation of Vlachopoulos and Diederichs [23] is used to approximate how shaft wall convergence varies with distance behind the excavation face. Using the fully unloaded shaft wall convergence and plastic zone radius from the unlined reference state under the same grouting and seepage conditions, this relation gives the following longitudinal displacement profile on the excavated side:

$$u(x) = u_{\max}\left\{1 - \left[1 - \frac{1}{3}\exp\left(-0.15\frac{R_{p,\max}}{r_0}\right)\right]\exp\left(-\frac{3x}{2R_{p,\max}}\right)\right\} \tag{61}$$

Here, x is the axial distance from the shaft bottom excavation face, and $u(x)$ is the shaft wall convergence at the corresponding position in the unlined reference state.

4.2.2. Lining Activation State and Rock–Lining Equilibrium

Under drained conditions, the equivalent radial pressure at the shaft wall is $P = P_{vir} + P_L$. When the lining starts to carry load, its installed configuration is taken as stress-free, with zero additional deformation and support pressure. Virtual support pressure decreases as the excavation face moves away. Once face confinement is fully released, $P_{vir} = 0$, and the radial pressure at the shaft wall equals the actual support pressure exerted by the lining. The rock–lining interaction is illustrated in Figure 6, and the final equilibrium state satisfies:

$$\begin{cases} P_{eq} - K_L\left[u_r(r_0;P_{eq}) - u_i\right] = 0 \\ u_{eq} = u_r(r_0;P_{eq}) \end{cases} \tag{62}$$

Here, P_{eq} and u_{eq} are the final equilibrium lining contact pressure and shaft wall convergence, respectively.

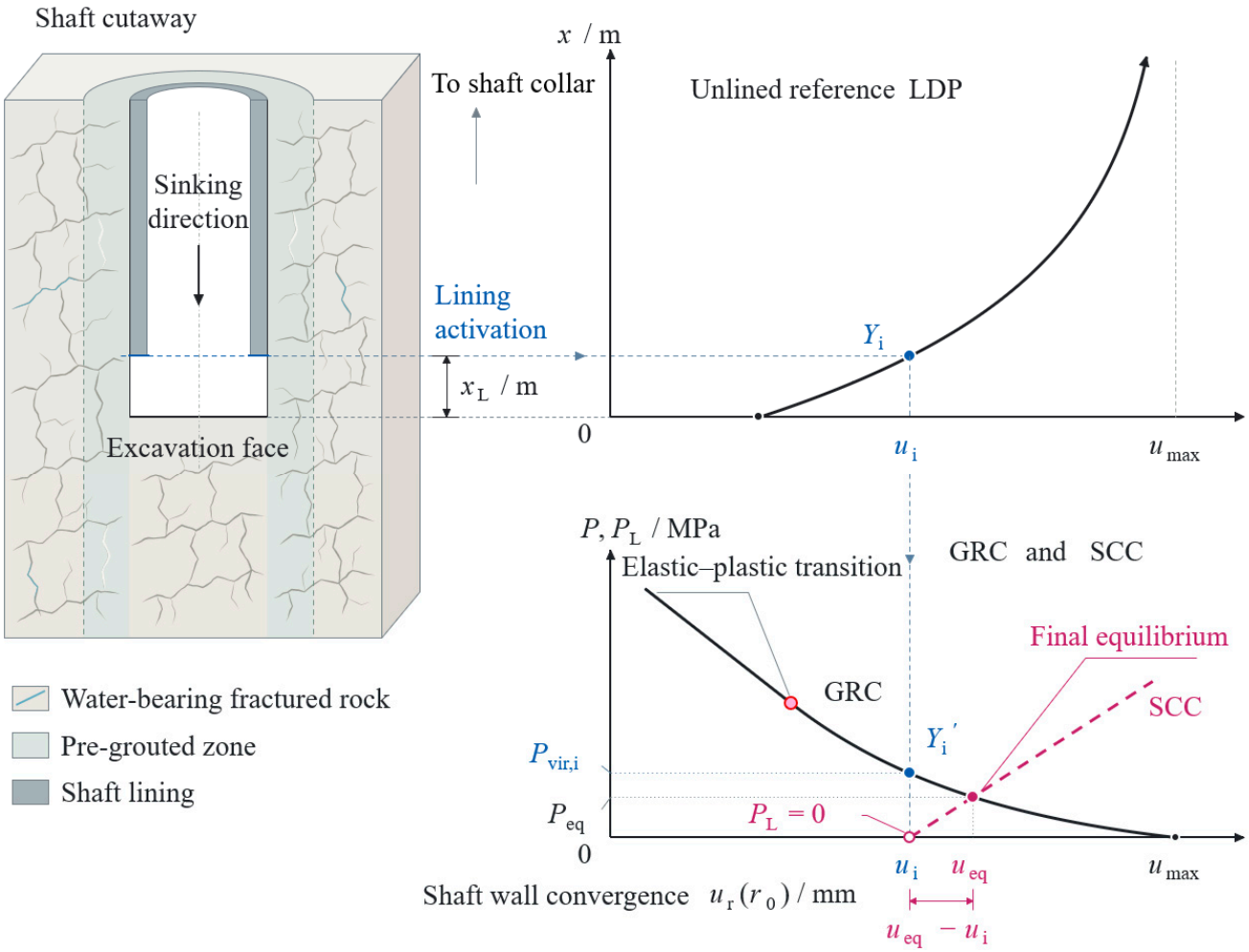


Figure 6. Rock–lining interaction in a pre-grouted shaft.

5. Results and Discussion

5.1. Rock–Lining Response and Sensitivity Analysis

The rock mass parameters in Table 1 are adopted. The lining thickness is $h_L = 0.6$ m, Young's modulus is $E_L = 34.5$ GPa, and Poisson's ratio is $\nu_L = 0.20$ [36]. The lining starts to carry load at a distance $x_L = 3.75$ m from the excavation face. A constant-stiffness linear-elastic model is used for the lining, giving a support stiffness $K_L = 1.73$ MPa/mm.

As shown in Figure 7, the unlined, zero-support-pressure reference state has a shaft wall convergence of 37.69 mm and a plastic zone radius of 4.42 m. The Vlachopoulos–Diederichs (V–D) relation gives the convergence at lining activation, $u_i = 30.07$ mm, corresponding to a virtual support pressure of 1.42 MPa on the GRC. The SCC starts at u_i and intersects the GRC at equilibrium point E, giving a lining contact pressure of 1.26 MPa, an equilibrium convergence of 30.80 mm, and an additional convergence after activation of 0.73 mm. Lining deformation under load is determined by the convergence increment after activation; deformation accumulated beforehand is excluded. The activation distance and lining stiffness determine the starting point and slope of the SCC, respectively, and jointly establish the equilibrium state.

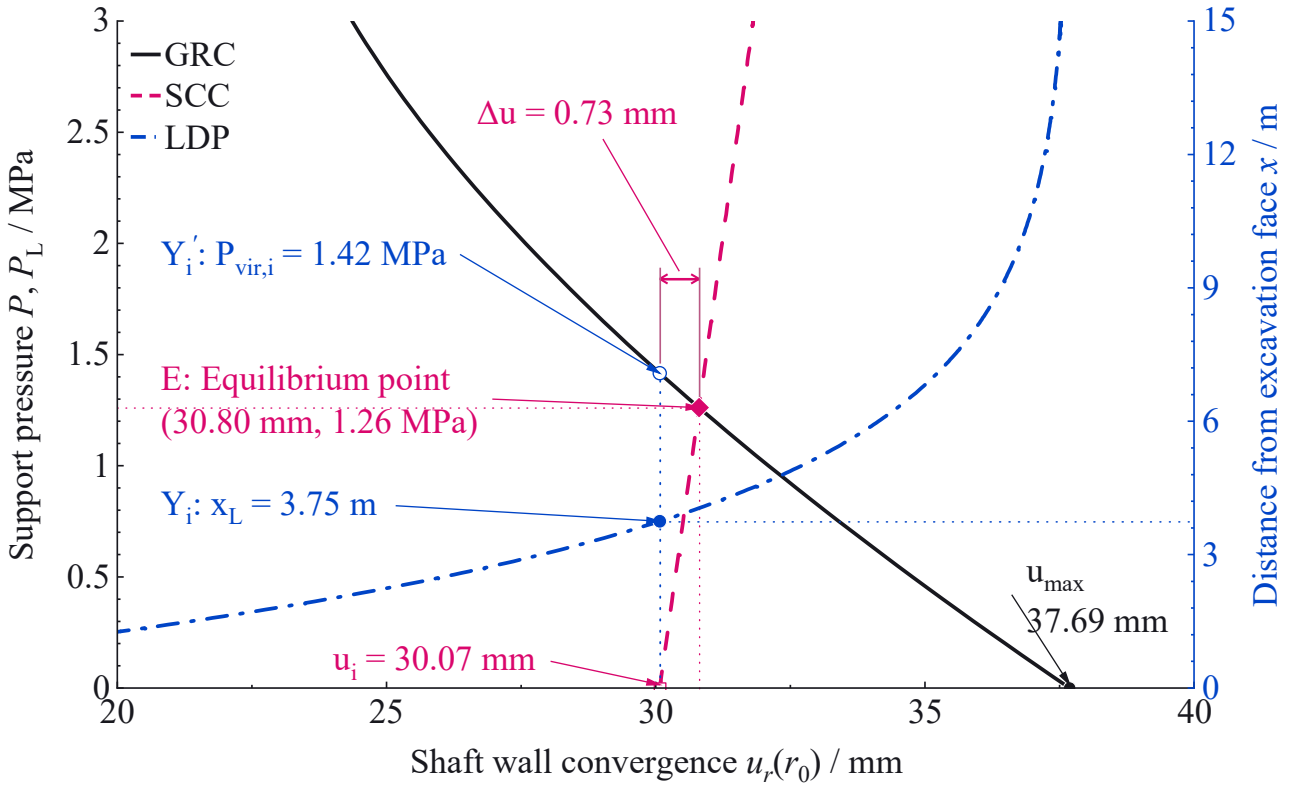


Figure 7. Combined GRC–LDP–SCC analysis for the baseline case.

Figure 8 shows the rock–lining response when the dilation angles in the grouted and ungrouted zones were set to 100%, 80%, and 50% of their respective baseline values. All other parameters were kept constant. At a virtual support pressure of 1 MPa, the shaft wall convergences were 32.10, 30.94, and 29.84 mm, respectively. At zero support pressure, the corresponding values were 37.69, 35.64, and 33.58 mm. The effect of the dilation angles on convergence was therefore more pronounced after complete unloading. For a lining thickness of 0.60 m and an activation distance of 3.75 m, the shaft wall convergences at lining activation were 30.07, 28.44, and 26.80 mm, respectively. The corresponding equilibrium convergences were 30.80, 29.25, and 27.75 mm, and the equilibrium lining contact pressures were 1.26, 1.41, and 1.65 MPa. Reducing the dilation angles to 80% and 50% of their baseline values reduced the equilibrium convergence by 5.03% and 9.91%, respectively. At zero support pressure, the plastic zone radius was 4.42 m in all three cases, and the plastic zone remained within the grouted zone.

Figure 9 compares the rock–lining response for four cases. These comprise the Darcy case $(m_1,m_0) = (1,1)$, the baseline non-Darcy case (1.05,1.01), and two cases in which both exponents were increased to 1.1 and 1.2 times their respective baseline values. The pore pressure boundary conditions were the same in all four cases. For each zone, the flow velocity at unit hydraulic gradient was held constant across the four cases. The pore pressures at the interface between the grouted and ungrouted zones were 5.37, 5.68, 6.04, and 6.34 MPa, respectively. The largest difference in pore pressure between the Darcy case and the case with exponents at 1.2 times their baseline values was 0.97 MPa and occurred at the interface. Across the sampled virtual support pressures, the maximum difference in shaft wall convergence between these two GRCs was 0.27 mm. For a lining thickness of 0.60 m and an activation distance of 3.75 m, the equilibrium convergence decreased from 30.86 to 30.68 mm between these two cases, and the equilibrium lining contact pressure decreased by 4.24 kPa (0.34%). Under the conditions examined, increasing the non-Darcy

exponents had a pronounced effect on the interface pore pressure and only a small effect on the equilibrium convergence and lining contact pressure.

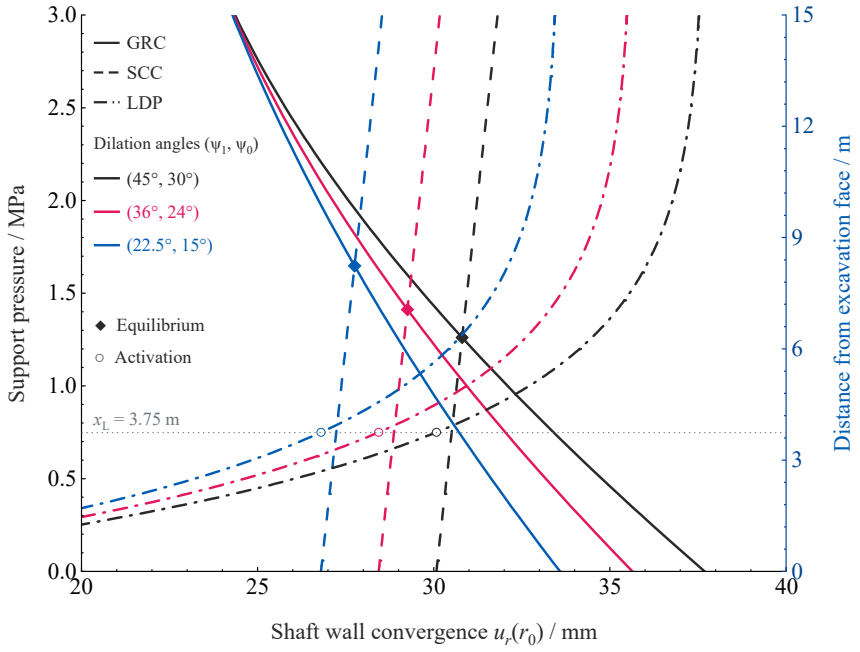


Figure 8. Effect of dilation angles on the rock–lining response.

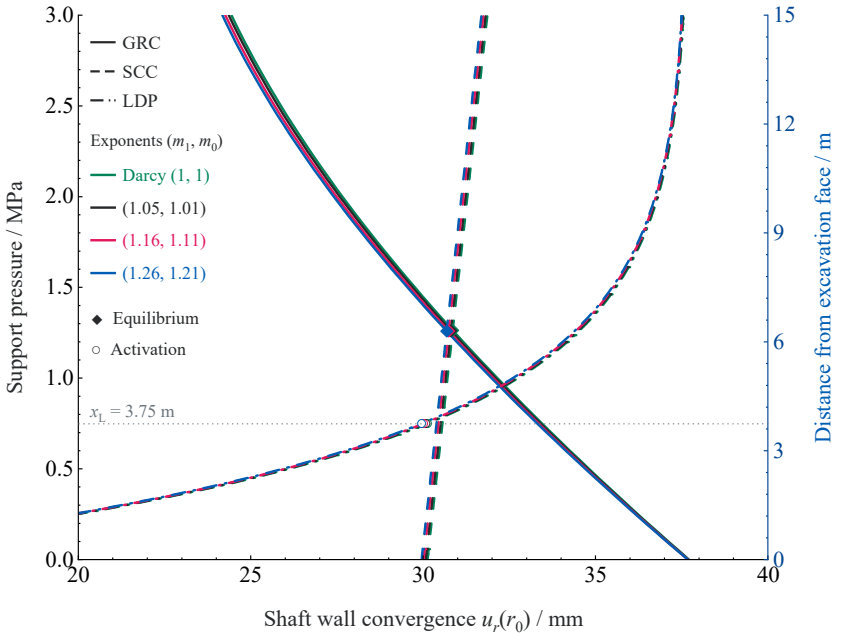


Figure 9. Effect of non-Darcy exponents on the rock–lining response.

5.2. Effects of Lining Activation Distance on Load and Deformation

Figure 10 shows the effect of varying x_L, the distance from the excavation face at which the lining starts to carry load. As x_L increases from 1.88 m (half the excavation radius) to 11.25 m, the equilibrium lining contact pressure decreases from 2.79 MPa to 0.09 MPa, whereas the equilibrium shaft wall convergence increases from 24.92 mm to 37.14 mm. The pressure reduction and convergence increase per increment of distance both diminish as the distance increases.

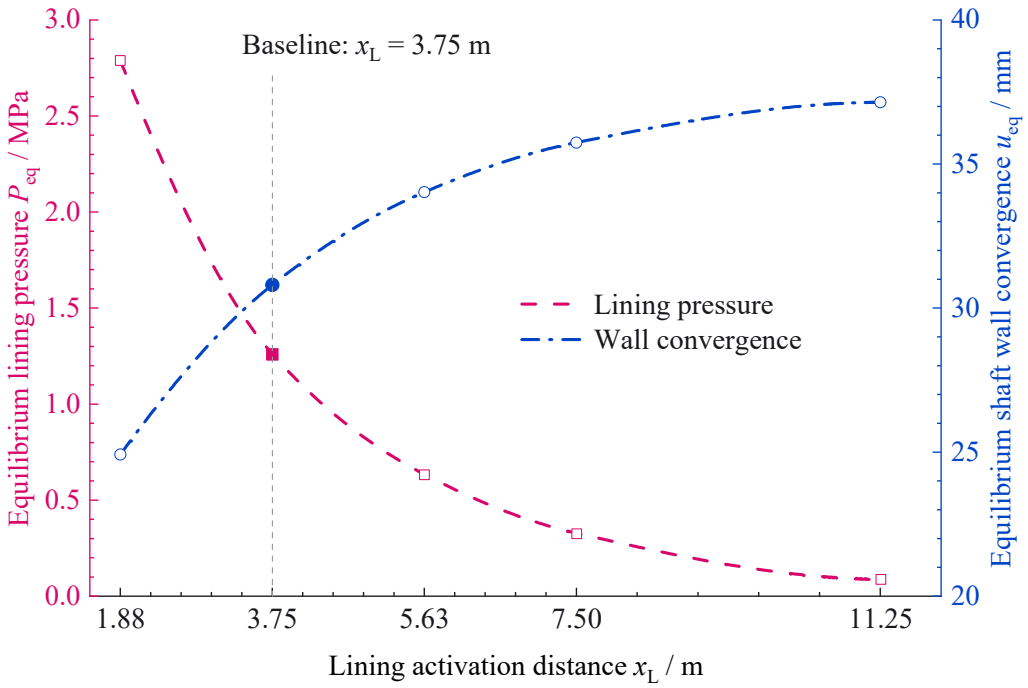


Figure 10. Effects of lining activation distance on equilibrium lining contact pressure and shaft wall convergence.

A larger activation distance allows greater rock mass convergence before the lining starts to carry load. This shifts the starting point of the SCC to the right and moves its intersection with the GRC toward lower pressure and greater convergence. Within the model and parameter range considered, increasing the activation distance therefore reduces the lining load but increases equilibrium shaft wall convergence. Selection of this distance must address both load and deformation-control requirements.

5.3. Effects of Pre-Grouting Parameters on the Lining Load Response

The lining activation distance is fixed at 3.75 m, while the lining stiffness and other parameters retain their baseline values. The effects of grouted-zone thickness, grouted-zone Young's modulus E_1, and cohesion c_1 are examined separately.

As shown in Figure 11, increasing the grouted-zone thickness from 2.25 m to 6.25 m reduces the equilibrium lining contact pressure and shaft wall convergence by 11.6% and 22.4%, respectively. The convergence increment after lining activation decreases from 0.79 mm to 0.70 mm. The plastic zone remains within the grouted zone in all these cases, so increasing the grouted-zone thickness extends the reinforced elastic region outside the plastic zone. Successive equal thickness increments produce progressively smaller reductions in pressure and convergence, indicating diminishing benefits from increasing the grouted-zone thickness.

As shown in Figure 12, increasing the grouted-zone Young's modulus E_1 from 2.10 GPa to 4.20 GPa reduces the equilibrium shaft wall convergence from 42.60 mm to 24.23 mm. The plastic zone radius in the unlined reference state remains approximately 4.42 m, and the ratio of convergence at lining activation to reference convergence remains approximately 79.8%. Thus, varying Young's modulus in these cases primarily reduces the deformation magnitude. Convergence at lining activation decreases with the reference deformation, whereas the subsequent convergence increment remains within 0.72–0.73 mm. The equilibrium lining contact pressure consequently varies only slightly, within 1.25–1.26 MPa.

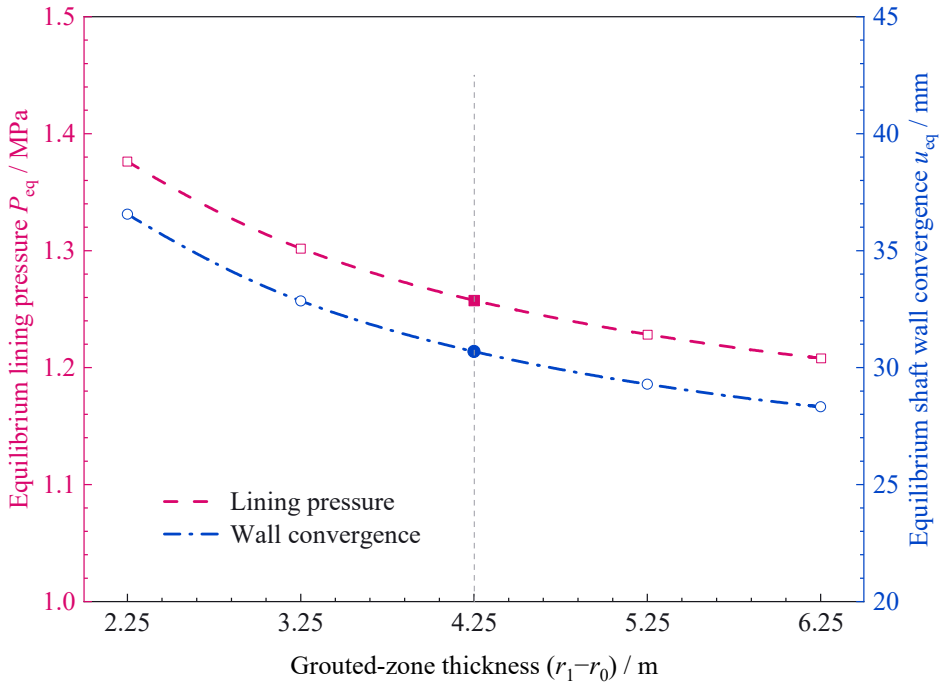


Figure 11. Effects of grouted-zone thickness on equilibrium lining contact pressure and shaft wall convergence.

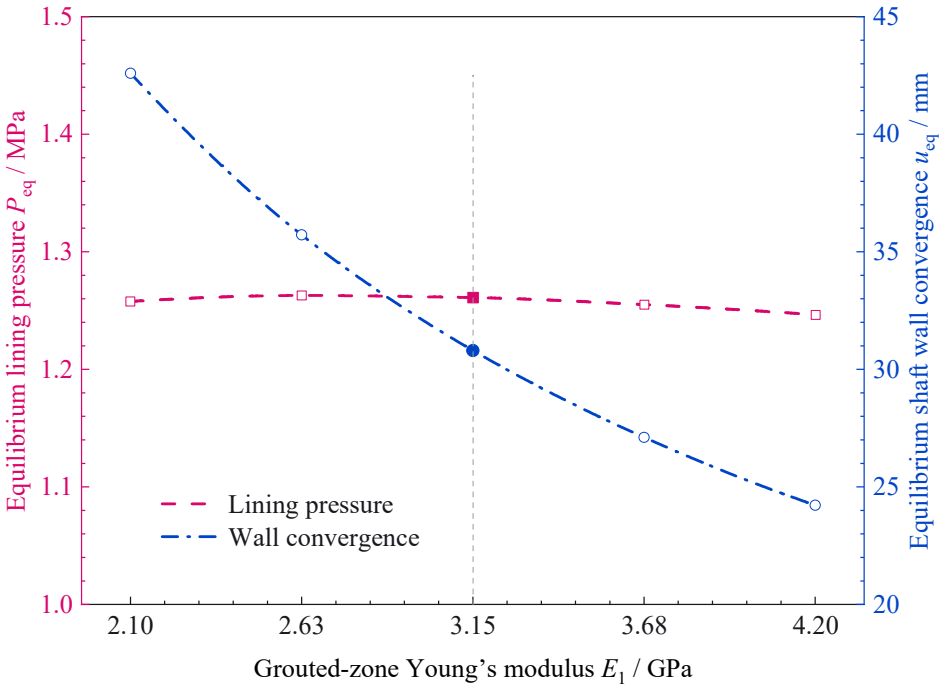


Figure 12. Effects of grouted-zone Young's modulus on equilibrium lining contact pressure and shaft wall convergence.

As shown in Figure 13, increasing the grouted-zone cohesion c_1 from 1.20 MPa to 2.00 MPa reduces the plastic zone radius in the unlined reference state from 4.50 m to 4.35 m and the equilibrium shaft wall convergence from 31.76 mm to 29.94 mm. This reflects the restriction of plastic zone development by the increased strength. According to the V–D relation, the smaller plastic zone increases the normalized convergence at lining activation from 79.3% to 80.2% at the same activation distance. The reduction in reference convergence lowers convergence at activation, while the increase in its normalized ratio partly offsets this

reduction. The calculated convergence increment after activation remains approximately 0.73 mm, and the equilibrium lining contact pressure remains approximately 1.26 MPa.

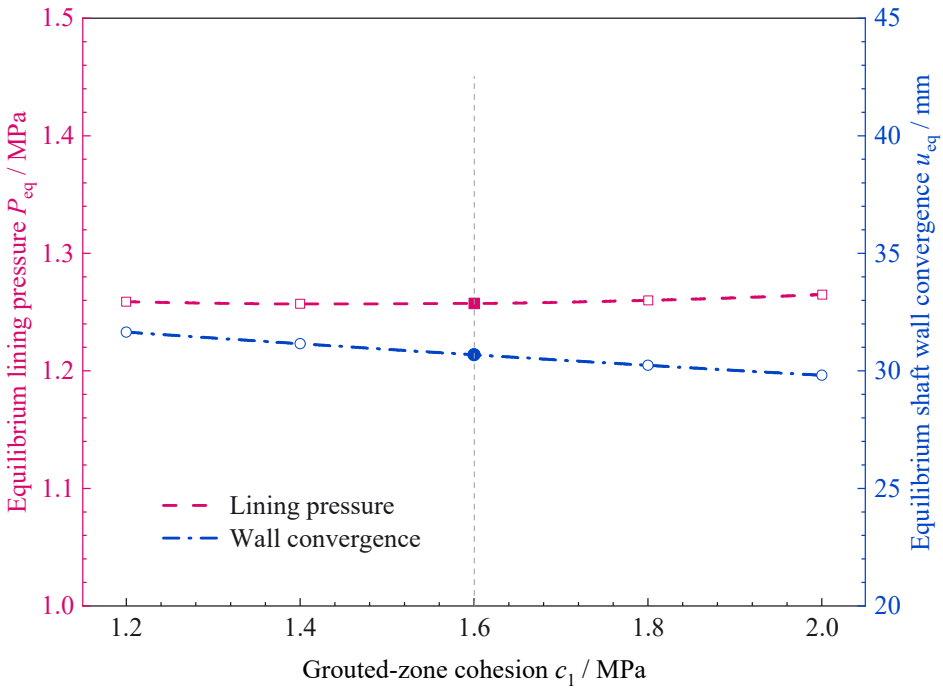


Figure 13. Effects of grouted-zone cohesion on equilibrium lining contact pressure and shaft wall convergence.

Equivalent reinforced zones have been incorporated into GRC models to represent the effect of ground reinforcement [21]. The GRC–LDP–SCC framework further relates ground deformation to support stiffness and installation position [22,23]. In the present analysis, grouting modifies both the GRC and the unlined reference state used to locate lining activation. Separating convergence before and after activation identifies the deformation component affected by each design variable. This explains the different lining-pressure sensitivities to grouting extent, stiffness, and strength, and provides the basis for comparing equal-convergence combinations in Section 6.

5.4. Discussion of Applicability and Limitations

The proposed method applies to deep circular shafts with a drained shaft wall, approximately axisymmetric in situ stresses, and a grouted zone that can be represented as a concentric homogeneous ring. It can be used for a preliminary comparison of grouting and lining support schemes. The plane-strain model uses the V–D relation for the unlined reference state to approximate the three-dimensional effect of the excavation face. If the actual longitudinal convergence profile deviates from this relation, the predicted shaft wall convergence at a given activation distance and the resulting lining contact pressure will both be affected. This deviation will also affect the activation distance back-calculated for a target convergence. Uneven grout filling of fractures can cause permeability and stiffness to vary around the shaft circumference. Fracture opening or closure during excavation-induced unloading may also alter local permeability and pore pressure distribution. The model represents the grouted zone as a homogeneous ring and accounts for the one-way effect of steady-state seepage on rock stress. It therefore has limited ability to capture local deformation and peak contact pressures in poorly grouted areas. The lining is modeled with constant elastic stiffness and is assumed to remain in compressive contact with the surrounding rock mass. If the lining begins to carry load at an early concrete

age, stiffness gain, creep, or cracking may alter the relationship between contact pressure and additional convergence after activation. These changes may affect the predicted equilibrium state.

Future studies could use three-dimensional simulations of staged excavation and measurements of shaft wall convergence at different distances from the excavation face to assess the displacement at lining activation predicted by the V–D relation. Measurements of pore pressure and convergence at different positions around the shaft circumference could be used to assess how the assumption of a homogeneous grouted ring affects local response predictions. Tests of the elastic modulus of concrete at different ages, combined with lining strain measurements, could also be used to assess whether the assumption of constant lining stiffness is appropriate during loading.

6. Joint Design of Grouting and Shaft Linings

6.1. Design Criteria and Computational Workflow

Lining thickness h_{L} and lining activation distance x_{L} are taken as the design variables. With the rock mass, hydraulic, and grouting parameters fixed, the unlined reference LDP is used to determine convergence at lining activation. The lining stiffness is updated and the GRC–SCC intersection is solved using the methods in Sections 4.1 and 4.2, giving the equilibrium contact pressure P_{eq} and shaft wall convergence u_{eq} for each combination. Here, x_{L} denotes the distance from the shaft bottom excavation face at which the lining starts to carry load.

The lining outer and inner radii are r_0 and $r_0 - h_L$, respectively. With zero radial pressure at the inner surface and uniform pressure at the outer surface, the design pressure $P_{L,d}$ is determined from the load combination adopted for the project. The maximum hoop compressive stress at the lining inner surface is:

$$\sigma_{\theta,L,d}^{\max} = \frac{2r_0^2 P_{L,d}}{r_0^2 - (r_0 - h_L)^2} \tag{63}$$

The load-bearing contribution of reinforcement is excluded, and the maximum hoop compressive stress at the inner surface is used for preliminary selection of lining thickness. Material properties are taken from the Code for Design of Concrete Structures [36]. The design axial compressive strength of C50 concrete is $f_{\mathrm{c}} = 23.1$ MPa, and the corresponding value for plain concrete is $f_{cc} = 0.85 f_c \approx 19.6$ MPa.

Equation (63), together with $\sigma_{\theta,L,d}^{\max} \le f_{cc}$, gives the external pressure criterion for a specified thickness:

$$P_{L,d}(h_L, x_L) \le P_{L,Rd}(h_L) = \frac{f_{cc}}{2}\left[1 - \left(1 - \frac{h_L}{r_0}\right)^2\right] \tag{64}$$

The design results presented here apply to drained shaft walls. For a watertight lining without drainage behind it, external water pressure may govern the check in Equation (64). In that case, the design external pressure $P_{\mathrm{L,d}}$ should account for both the water pressure behind the lining and the load transmitted by the rock skeleton. If a project-specific allowable convergence u_{lim} is specified, $u_{\mathrm{eq}} \le u_{\mathrm{lim}}$ must also be satisfied. The lining inner radius and activation distance must meet clearance and construction requirements. Each combination is solved and checked following the workflow in Figure 14, and the thickness–distance combinations satisfying the selected criteria are retained. The external pressure criterion above is used for preliminary thickness selection under axisymmetric radial compression.

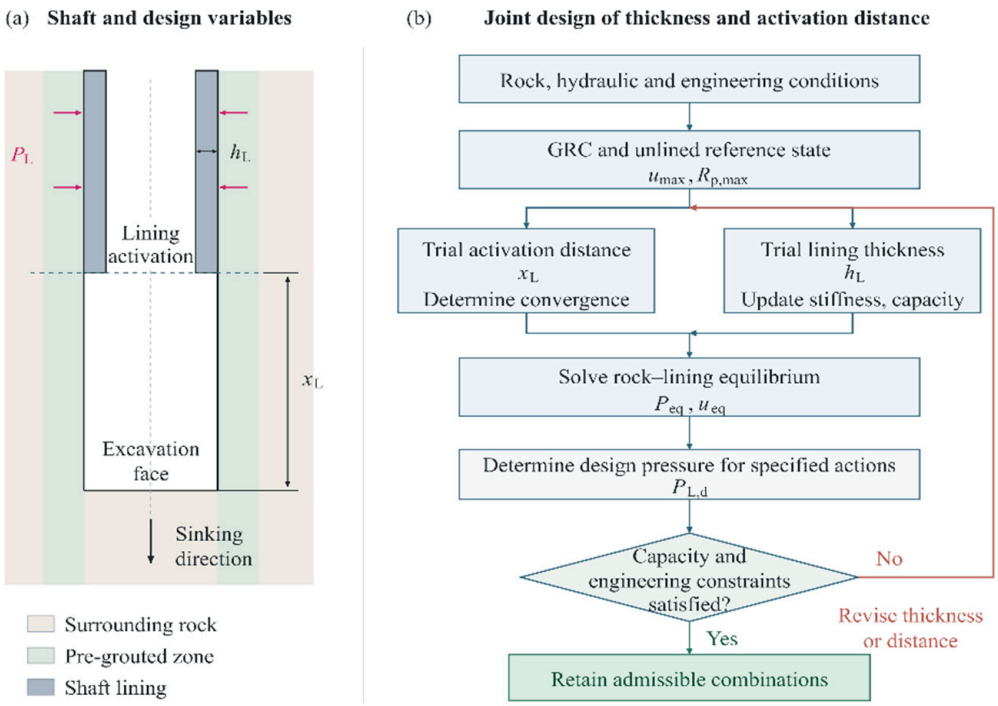


Figure 14. Workflow for joint design of lining thickness and activation distance.

6.2. Joint Response to Lining Thickness and Activation Distance

With the grouted-zone outer radius fixed at $r_1 = 8$ m and the other baseline parameters unchanged, 25 combinations of lining thickness $h_L = 0.30$–0.90 m and activation distance $x_L = 1.88$–11.25 m are calculated, as shown in Figure 15. At the same activation distance, increasing lining thickness increases the SCC slope and shifts the equilibrium point upward and to the left along the GRC. For example, at $x_L = 3.75$ m, increasing the thickness from 0.30 m to 0.90 m raises the equilibrium lining contact pressure from 1.13 MPa to 1.31 MPa and reduces shaft wall convergence from 31.46 mm to 30.55 mm, reflecting the greater confinement provided by the stiffer lining.

The convergence reduction achieved by increasing lining thickness diminishes as the activation distance increases. For the same thickness increase described above, the convergence reductions are 1.83 mm and 0.07 mm at activation distances of 1.88 and 11.25 m, respectively. In this model, a larger activation distance brings convergence at activation closer to the final convergence of the unlined reference state, leaving less subsequent convergence to be controlled by a thicker lining. The deformation-control effect of thickness adjustment therefore depends on the position at which the lining starts to carry load.

The pressure contours shift toward larger activation distances as lining thickness increases, showing how these two variables can be matched at a specified response level. On a common GRC, the same equilibrium pressure corresponds to the same shaft wall convergence. Candidate thickness–distance combinations with equal responses can therefore be constructed along the contours and then screened using the load-bearing and deformation criteria in Section 6.1, together with shaft clearance and construction requirements.

To assess the influence of the V–D relation on the design results, we varied the displacement at lining activation (u_i). At each lining activation distance, we set u_i to 80%, 90%, 100%, 110%, and 120% of the corresponding V–D estimate. Table 2 presents the results.

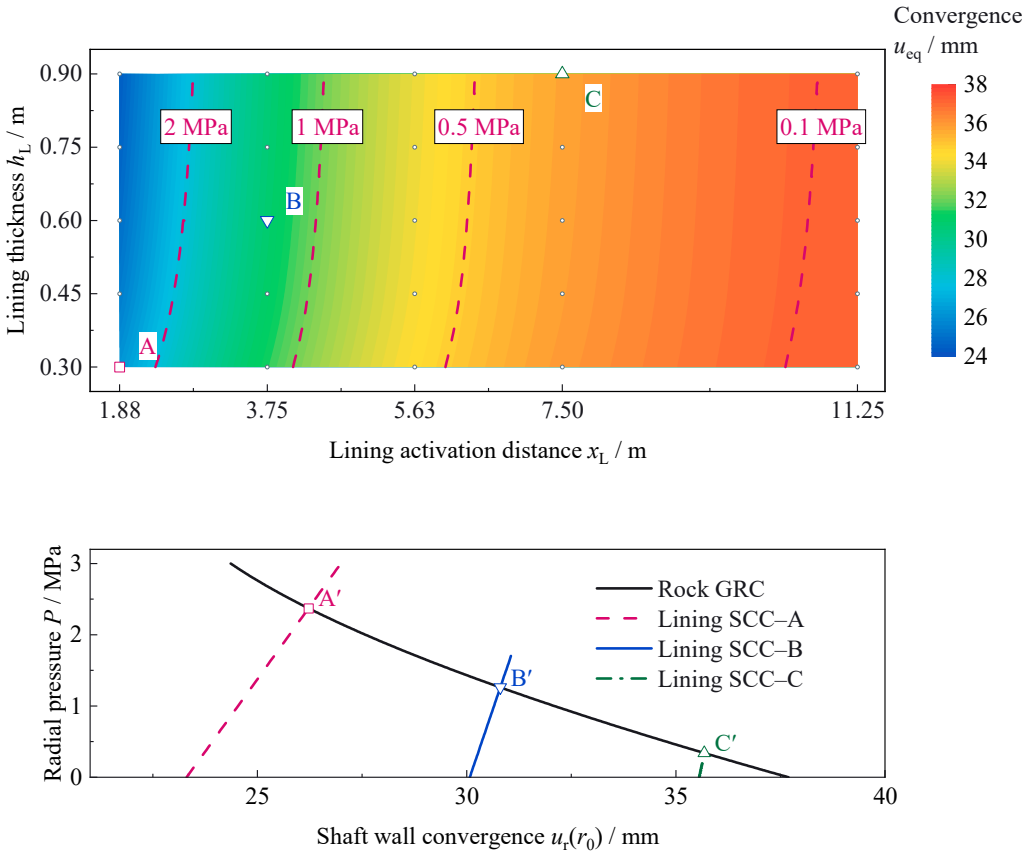


Figure 15. Joint response to lining thickness and activation distance and equilibrium states of representative combinations. The symbols indicate three representative combinations (A–C) and their corresponding equilibrium points (A′–C′).

Table 2. Effect of displacement at lining activation on equilibrium contact pressure and shaft wall convergence.

Relative Change in u_i	Displacement at Lining Activation, u_i (mm)	Equilibrium Contact Pressure (MPa)	Equilibrium Shaft Wall Convergence (mm)
−20%	24.06	2.58	25.55
−10%	27.07	1.86	28.14
0%	30.07	1.26	30.80
+10%	33.08	0.73	33.50
+20%	36.09	0.24	36.23

In the baseline case, reducing u_i by 10% relative to the V–D estimate increased the equilibrium contact pressure by 47.4% and reduced the equilibrium shaft wall convergence by 8.6%. Increasing u_i by 10% reduced the contact pressure by 42.1% and increased the convergence by 8.8%. In relative terms, the contact pressure was more sensitive to the estimate of u_i than the equilibrium convergence. Allowing moderate shaft wall convergence before the lining begins to carry load can reduce the load on the lining. The extent of this deformation should be limited so that the final convergence remains within the allowable limit. At each perturbation level, the cases with compressive rock–lining contact showed the same trend. Increasing the lining thickness produced a greater reduction in convergence at shorter activation distances.

6.3. Comparison of Equal-Convergence Combinations for Different Pre-Grouting Schemes

The equilibrium shaft wall convergence of the baseline case (r_1 = 8 m, h_L = 0.60 m, and x_L = 3.75 m) is used as the target. Its value is approximately 30.80 mm. The outer radius of the grouted zone, r_1, takes values of 7, 8, and 9 m. The lining thickness, h_L, takes values of 0.30, 0.60, and 0.90 m. All other material and loading parameters retain their baseline values. For each grouting radius, the ground reaction curve (GRC) and the unsupported reference state are recalculated. Starting from zero, the support pressure is increased in steps of 0.25 MPa to bracket the target convergence on the selected monotonic branch of the GRC. A bracketing method is then used to find the corresponding equilibrium contact pressure P_{eq}. For a given lining thickness, the support characteristic curve (SCC) gives the displacement at lining activation as $u_i = u_{eq} - P_{eq}/K_L$. The V–D relation on the excavated side of the face is then inverted to obtain the lining activation distance x_L. For each retained combination, u_i lies within the range of this relation, and x_L lies between one-half and three times the excavation radius. The inverse and forward calculations each give an equilibrium convergence that differs from the target by less than 0.01 mm. For a fixed grouting scheme and lining thickness, the matched distance is unique whenever a feasible solution exists because the V–D relation is strictly monotonic on the excavated side. Different grouting radii or lining thicknesses can yield different combinations that meet the same convergence target. Figure 16 shows the nine matched combinations.

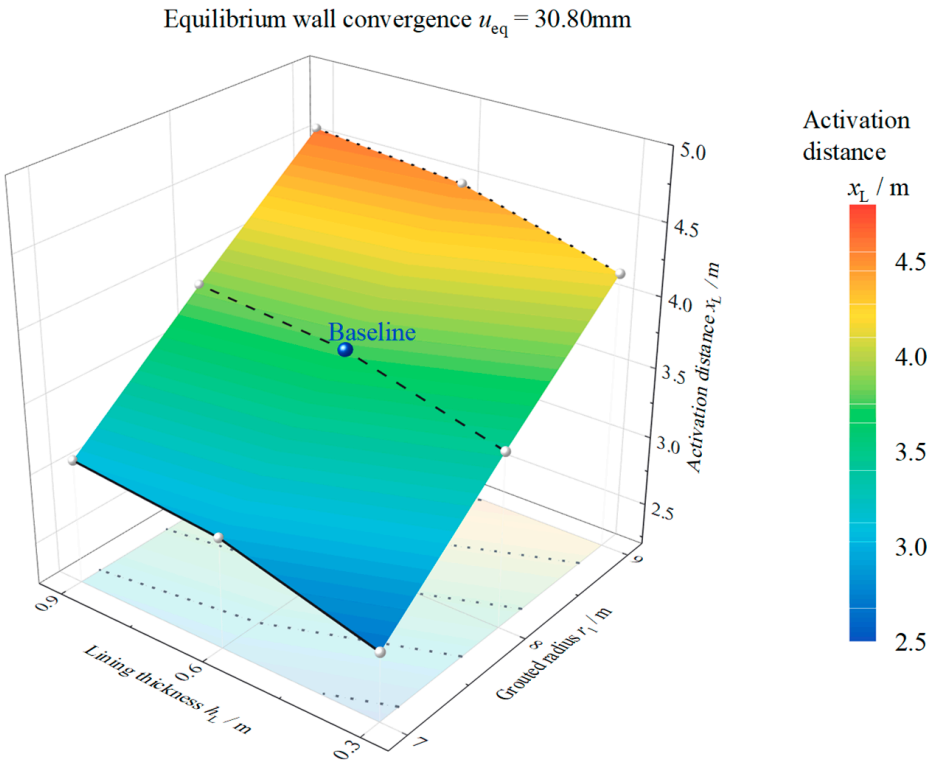


Figure 16. Matching grouted-zone outer radius, lining thickness, and activation distance at equal convergence. The black lines connect cases with the same grouted-zone radius, and the gray dotted lines indicate activation-distance contours.

For a lining thickness of 0.60 m, increasing the grouted-zone outer radius from 7 m to 9 m increases the matching activation distance from 2.99 m to 4.47 m, an increase of 49.6%, and reduces the equilibrium lining contact pressure from 1.75 MPa to 0.94 MPa, a reduction of 46.3%. At the same convergence level, the larger grouting extent lowers the support pressure on the GRC, reducing the deformation required after lining activation to

reach equilibrium. Together with the deformation distribution of each unlined reference state, this allows lining activation farther from the excavation face.

With the grouted-zone outer radius fixed at 8 m, lining thicknesses of 0.30, 0.60, and 0.90 m give matching activation distances of 3.45, 3.75, and 3.86 m, respectively. The two equal thickness increments increase the matching distance by 0.30 m and 0.11 m, respectively, indicating a diminishing distance gain in this example. For the same grouting scheme and target convergence, the equilibrium pressure is determined by the same GRC. A thicker lining increases stiffness and reduces the deformation needed after activation to develop this pressure, allowing a larger convergence at activation and a greater activation distance.

For a specified activation distance, candidate combinations of grouting extent and lining thickness can be compared along the constant-distance contours on the base plane. They can then be screened against the strength, clearance, and construction requirements in Section 6.1.

For the nine equal-convergence schemes, the equilibrium shaft wall convergence of each scheme is first compared with the project-specific allowable value. If the target convergence exceeds this limit, the target should be reduced and the parameters matched again. If the convergence requirement is met, the schemes can be further screened against the groundwater inflow and lining capacity requirements. For grouted-zone outer radii of 7, 8, and 9 m, the groundwater inflows per unit shaft depth are 0.23, 0.20, and 0.19 $m^3/(h{\cdot}m)$, respectively. If the allowable inflow lies between the values calculated for the 7 m and 8 m schemes, the 7 m scheme can be excluded and the 8 m and 9 m schemes retained. For a grouted-zone outer radius of 8 m, lining thicknesses of 0.30 and 0.60 m give matching activation distances of 3.45 and 3.75 m, respectively. The corresponding external pressure capacities calculated using Equation (64) are 1.51 and 2.89 MPa. If the design external pressure determined from the project load combination exceeds 1.51 MPa but does not exceed 2.89 MPa, only the 0.60 m lining satisfies the capacity requirement among the two candidates.

7. Conclusions

The GRC, V–D longitudinal displacement relation, and lining SCC are combined to analyze the interaction between pre-grouted rock masses and shaft linings under high water pressure. The effects of pre-grouting parameters, lining activation distance, and lining thickness on the equilibrium response are examined. The main conclusions are as follows.

(1) Increasing the grouting extent reduces both equilibrium shaft wall convergence and lining contact pressure, with diminishing benefits from increasing the grouted-zone thickness. At a lining activation distance of 3.75 m and a lining thickness of 0.60 m, increasing the grouted-zone thickness from 2.25 m to 6.25 m reduces equilibrium shaft wall convergence and lining contact pressure by 22.4% and 11.6%, respectively. Increasing the grouted-zone thickness from 2.25 to 3.25 m reduces equilibrium shaft wall convergence and lining contact pressure by 3.68 mm and 0.07 MPa, respectively, whereas the corresponding reductions from 5.25 to 6.25 m are only 0.97 mm and 0.02 MPa. Increasing the Young's modulus or cohesion of the grouted zone primarily reduces convergence before lining activation.

(2) Increasing the lining activation distance reduces lining contact pressure but increases equilibrium shaft wall convergence, with progressively smaller changes in both quantities per increment of distance. For a grouted-zone outer radius of 8 m and a lining thickness of 0.60 m, increasing the activation distance from 1.88 m to 11.25 m reduces lining contact pressure from 2.79 MPa to 0.09 MPa and increases equilibrium shaft wall convergence from 24.92 mm to 37.14 mm. The greater convergence accumulated before activation leaves less subsequent deformation to be constrained by the lining.

(3) The convergence-control benefit of increasing lining thickness diminishes as the lining activation distance increases. Increasing lining thickness from 0.30 m to 0.90 m reduces equilibrium shaft wall convergence by 1.83 mm and 0.07 mm at activation distances of 1.88 m and 11.25 m, respectively. As convergence at activation approaches the final convergence of the unlined reference state, less deformation remains to be controlled by increasing lining stiffness.

(4) A common equilibrium convergence provides a basis for matching grouting extent, lining thickness, and lining activation distance. At an equilibrium convergence of 30.80 mm and a lining thickness of 0.60 m, increasing the grouted-zone outer radius from 7 m to 9 m increases the matching activation distance from 2.99 m to 4.47 m, an increase of 49.6%, and reduces lining contact pressure from 1.75 MPa to 0.94 MPa, a reduction of 46.3%. A larger grouting extent therefore permits a lower lining load and a greater matching activation distance while maintaining the same convergence level.

Author Contributions: Conceptualization, S.Z.; methodology, W.L. and X.Z.; software, W.M.; validation, Y.L. and J.D.; formal analysis, Y.L., S.Z. and W.M.; writing—original draft preparation, Y.L. and W.L.; writing—review and editing, S.Z. and W.L.; supervision, S.Z.; project administration, X.Z.; funding acquisition, S.Z., X.Z. and J.D. All authors have read and agreed to the published version of the manuscript.

Funding: This research was funded by the National Natural Science Foundation of China (grant number U24B2039) and the Natural Science Foundation of Hebei Province (grant number E2025404012).

Data Availability Statement: The data supporting the findings of this study are available from the corresponding author upon reasonable request.

Conflicts of Interest: Author Wei Li was employed by the company Hebei Zhucheng Industrial and Mining Machinery Co., Ltd. The remaining authors declare that the research was conducted in the absence of any commercial or financial relationships that could be construed as a potential conflict of interest.

Nomenclature

Symbol	Definition	Unit
r, x	Radial and axial coordinates	m
r_0, r_1, r_2	Shaft radius, grouted-zone outer radius, recharge radius	m
R_p, $R_{p,max}$	Plastic zone radius and its fully unloaded, unlined value	m
P_{w0}, P_{w1}, P_{w2}	Pore pressure at wall, grout interface and recharge boundary	MPa
q	Groundwater inflow per unit shaft depth	m^2/s
m_j	Non-Darcy exponent	–
k_j	Izbash coefficient	$(m/s)^{m_j}$
λ	Effective stress correction coefficient	–
σ'_r, σ'_θ	Radial and hoop effective stresses	MPa
P_{vir}	Virtual support pressure	MPa
E_j, G_j	Rock Young's and shear moduli	GPa
E_L	Lining Young's modulus	GPa
ν_j, ν_L	Rock and lining Poisson's ratios	–
c_j	Rock cohesion	MPa
φ_j, ψ_j	Friction and dilation angles	°
P_L, P_{eq}	Lining contact pressure, current and at equilibrium	MPa
u_i, u_{eq}, u_{lim}	Shaft wall convergence at activation and equilibrium, and its allowable limit	mm
h_L, x_L	Lining thickness and activation distance	m
K_L	Radial lining stiffness	MPa/mm
$P_{L,d}$, $P_{L,Rd}$	Design external pressure and lining capacity	MPa
j	j = 1 denotes grouted rock and j = 0 denotes ungrouted rock.	—

References

1. Ranjith, P.G.; Zhao, J.; Ju, M.; De Silva, R.V.S.; Rathnaweera, T.D.; Bandara, A.K.M.S. Opportunities and Challenges in Deep Mining: A Brief Review. *Engineering* **2017**, *3*, 546–551. [CrossRef]
2. Shakeri, J.; Ghorbani, E.; Taheri, A. A review of deep mining challenges, hazard mitigation, design approaches, and support methods. *Undergr. Space* **2026**, *28*, 86–136. [CrossRef]
3. Hashemi, S.; Ashcroft, B.; Chittenden, N.; Gwildis, U.; Heine, J.; Luxford, J.; Marquis, F.; Nasri, V.; Preene, M.; Shaterpour-Mamaghani, A.; et al. Selection of shaft construction method. *Tunn. Undergr. Space Technol.* **2025**, *164*, 106654. [CrossRef]
4. Wang, C.; Friedman, M.; Wu, W.; Zhang, D.; Li, Z. Hydraulic influences on the long-term performance of tunnels: A review. *Transp. Geotech.* **2024**, *48*, 101329. [CrossRef]
5. Oreste, P.; Spagnoli, G.; Lo Bianco, L. A Combined Analytical and Numerical Approach for the Evaluation of Radial Loads on the Lining of Vertical Shafts. *Geotech. Geol. Eng.* **2016**, *34*, 1057–1065. [CrossRef]
6. Wang, X.; Tan, Z.; Wang, M.; Zhang, M.; Ming, H. Theoretical and experimental study of external water pressure on tunnel lining in controlled drainage under high water level. *Tunn. Undergr. Space Technol.* **2008**, *23*, 552–560. [CrossRef]
7. Zhou, X.; Xu, Y.; Liu, S.; He, X. Research on stress and seepage fields of surrounding rock grouting of ultra-deep shafts of gold mines. *Chin. J. Rock Mech. Eng.* **2020**, *39*, 1611–1621. (In Chinese) [CrossRef]
8. Kang, H.; Li, W.; Gao, F.; Yang, J. Grouting theories and technologies for the reinforcement of fractured rocks surrounding deep roadways. *Deep Undergr. Sci. Eng.* **2023**, *2*, 2–19. [CrossRef]
9. Feng, Z.; Zhang, Z.; Tang, Q.; Zhou, Y. Mechanical properties and microscopic research of different types of bentonite in conjunction with cement and fine sand. *Soils Found.* **2025**, *65*, 101573. [CrossRef]
10. Tang, Q.; Tian, A.; Ling, C.; Huang, Y.; Gu, F. Physical and mechanical properties of recycled aggregates modified by microbially induced calcium carbonate precipitation. *J. Clean. Prod.* **2023**, *382*, 135409. [CrossRef]
11. Chen, Y.; Tang, Q.; Zhang, Z.; Pan, X.; Kawasaki, S. Erosion resistance and hydrological response of the slope enhanced by enzyme-induced calcium carbonate precipitation. *J. Rock Mech. Geotech. Eng.* **2026**, *18*, 3555–3570. [CrossRef]
12. Langford, J.; Holmøy, K.H.; Hansen, T.F.; Holter, K.G.; Stein, E. Analysis of water ingress, grouting effort, and pore pressure reduction caused by hard rock tunnels in the Oslo region. *Tunn. Undergr. Space Technol.* **2022**, *130*, 104762. [CrossRef]
13. Li, Z.; Liu, H.; Dun, Z.; Ren, L.; Fang, J. Grouting effect on rock fracture using shear and seepage assessment. *Constr. Build. Mater.* **2020**, *242*, 118131. [CrossRef]
14. Zhang, G.-S.; Xiao, M.-L.; Zhang, Y.-D.; Liu, H.-Z.; Zhuo, L.; Xie, H.-Q.; He, J.-D. Experimental and numerical study on the mechanical properties of compressively precracked sandstone repaired by grouting. *Constr. Build. Mater.* **2022**, *350*, 128816. [CrossRef]
15. Zhang, Y.; Zhang, D.; Fang, Q.; Xiong, L.; Yu, L.; Zhou, M. Analytical solutions of non-Darcy seepage of grouted subsea tunnels. *Tunn. Undergr. Space Technol.* **2020**, *96*, 103182. [CrossRef]
16. Zheng, L.; Zhang, D.; Sun, Z.; Lu, S.; Du, Y. Non-Darcy seepage analysis on subsea tunnel in fractured rock mass with grouting reinforcement. *Tunn. Undergr. Space Technol.* **2026**, *168*, 107115. [CrossRef]
17. He, X.-N.; Zhou, X.-M.; Guo, X.-H.; Xu, Y.; Ma, W.-Z. Analysis of Non-Darcy Seepage Field and Stress Field of Surrounding Rock Strengthened by Grouting in Deep Buried Tunnel. *China J. Highw. Transp.* **2020**, *33*, 200–211. (In Chinese) [CrossRef]
18. Carranza-Torres, C.; Zhao, J. Analytical and numerical study of the effect of water pressure on the mechanical response of cylindrical lined tunnels in elastic and elasto-plastic porous media. *Int. J. Rock Mech. Min. Sci.* **2009**, *46*, 531–547. [CrossRef]
19. Shin, Y.-J.; Song, K.-I.; Lee, I.-M.; Cho, G.-C. Interaction between tunnel supports and ground convergence—Consideration of seepage forces. *Int. J. Rock Mech. Min. Sci.* **2011**, *48*, 394–405. [CrossRef]
20. Jia, J.; Chen, Y.; Luo, H.; Ma, G. Seepage stability analysis of a deep-buried tunnel in fractured rocks based on a non-Darcy hydro-mechanical coupled method. *Tunn. Undergr. Space Technol.* **2023**, *142*, 105393. [CrossRef]
21. Fang, Q.; Zhang, D.; Zhou, P.; Wong, L.N.Y. Ground reaction curves for deep circular tunnels considering the effect of ground reinforcement. *Int. J. Rock Mech. Min. Sci.* **2013**, *60*, 401–412. [CrossRef]
22. Carranza-Torres, C.; Fairhurst, C. Application of the Convergence-Confinement method of tunnel design to rock masses that satisfy the Hoek-Brown failure criterion. *Tunn. Undergr. Space Technol.* **2000**, *15*, 187–213. [CrossRef]
23. Vlachopoulos, N.; Diederichs, M.S. Improved Longitudinal Displacement Profiles for Convergence Confinement Analysis of Deep Tunnels. *Rock Mech. Rock Eng.* **2009**, *42*, 131–146. [CrossRef]
24. Spagnoli, G.; Oreste, P.; Lo Bianco, L. New Equations for Estimating Radial Loads on Deep Shaft Linings in Weak Rocks. *Int. J. Geomech.* **2016**, *16*, 06016006. [CrossRef]
25. Spagnoli, G.; Oreste, P.; Lo Bianco, L. Estimation of Shaft Radial Displacement beyond the Excavation Bottom before Installation of Permanent Lining in Nondilatant Weak Rocks with a Novel Formulation. *Int. J. Geomech.* **2017**, *17*, 04017051. Correction in *Int. J. Geomech.* **2017**, *17*, 08217002. https://doi.org/10.1061/(ASCE)GM.1943-5622.0001036. [CrossRef]
26. Liu, H.; Tan, Z.; Wang, X.; Liu, X.; Zhao, X.; Li, Y. Sequential stress control and delayed support in deep shaft construction. *Arab. J. Geosci.* **2022**, *15*, 368. [CrossRef]

27. Chen, B.; Mo, P.; Lu, Z.; Kuang, L.; Zhang, Q.; Eslami, A. Semi-analytical solution for the stability of deep vertical shaft considering time-dependent rock-structure interaction. *Deep Undergr. Sci. Eng.* **2026**, *5*, 767–786. [CrossRef]
28. Kang, J.; Xie, H.; Lin, P.; Xu, Z. An integrated determination method of optimal supporting time against TBM jamming. *Eng. Fail. Anal.* **2024**, *162*, 108355. [CrossRef]
29. Carranza-Torres, C.; Rysdahl, B.; Kasim, M. On the elastic analysis of a circular lined tunnel considering the delayed installation of the support. *Int. J. Rock Mech. Min. Sci.* **2013**, *61*, 57–85. [CrossRef]
30. Oke, J.; Vlachopoulos, N.; Diederichs, M. Improvement to the Convergence-Confinement Method: Inclusion of Support Installation Proximity and Stiffness. *Rock Mech. Rock Eng.* **2018**, *51*, 1495–1519. [CrossRef]
31. De La Fuente, M.; Taherzadeh, R.; Sulem, J.; Nguyen, X.-S.; Subrin, D. Applicability of the Convergence-Confinement Method to Full-Face Excavation of Circular Tunnels with Stiff Support System. *Rock Mech. Rock Eng.* **2019**, *52*, 2361–2376. [CrossRef]
32. Sheng, Y.-M.; Wang, D.; Zou, J.-F.; Li, P. Semi-analytical characterization for the plastic development of deep-buried and water-rich non-circular tunnels considering out-of-plane stress based on three-dimensional strength criteria. *Tunn. Undergr. Space Technol.* **2026**, *167*, 107026. [CrossRef]
33. Guan, Z.; Jiang, Y.; Tanabasi, Y. Ground reaction analyses in conventional tunnelling excavation. *Tunn. Undergr. Space Technol.* **2007**, *22*, 230–237. [CrossRef]
34. Li, Z.-Y.; Zeng, Y.-H. *Design Principle and Method of Underground Structures*; Southwest Jiaotong University Press: Chengdu, China, 2003. (In Chinese)
35. Benato, A.; Gaida, E.; Oggeri, C.; Oreste, P. Analysis of the Importance of the Filling Material Characteristics Injected Around the Precast Concrete Lining in the Microtunnelling Technology. *Geotech. Geol. Eng.* **2023**, *41*, 2775–2785. [CrossRef]
36. *GB/T 50010-2010*; Code for Design of Concrete Structures (2024 Edition). China Architecture & Building Press: Beijing, China, 2024. (In Chinese)

Disclaimer/Publisher's Note: The statements, opinions and data contained in all publications are solely those of the individual author(s) and contributor(s) and not of MDPI and/or the editor(s). MDPI and/or the editor(s) disclaim responsibility for any injury to people or property resulting from any ideas, methods, instructions or products referred to in the content.